Research Square

Preprints are preliminary reports that have not undergone peer review.
They should not be considered conclusive, used to inform clinical practice,
or referenced by the media as validated information.

Beam-triggered chemical activation in deep aqueous media using laser-wakefield- accelerated electron beams

Tomonao Hosokai

hosokai@sanken.osaka-u.ac.jp

The University of Osaka

Yasunobu Yamashita
The University of Osaka

Yoshio Mizuta
The University of Osaka

Yusa Muroya
The University of Osaka

Toshiya Muto
The University of Osaka

Yan-Jun Gu
The University of Osaka

Kazumi Nakano
The University of Osaka

Kazumasa Minami
The University of Osaka

Keisuke Naito
The University of Osaka

Jinfeng Yang
The University of Osaka

Masahiko Koizumi
The University of Osaka

Yutaka Takahashi
The University of Osaka

Takayoshi Suzuki
The University of Osaka

Zhan Jin
The University of Osaka

Article

Keywords:

Posted Date: September 24th, 2026

DOI: https://doi.org/10.21203/rs.3.rs-10927279/v1

License: This work is licensed under a Creative Commons Attribution 4.0 International License.
Read Full License

Additional Declarations: No competing interests reported.

Beam-triggered chemical activation in deep aqueous media using laser-wakefield-accelerated electron beams

Tomonao Hosokai[1,2,3*], Yasunobu Yamashita[1,2,3*], Yoshio Mizuta[1,2,3], Yusa Muroya[1,2,3], Toshiya Muto[1,2,3], Yan-Jun Gu[1,2,3], Kazumi Nakano[1], Kazumasa Minami[4,1], Keisuke Naito[1], Jinfeng Yang[1,2], Masahiko Koizumi[4,1], Yutaka Takahashi[4,1], Takayoshi Suzuki[1], and Zhan Jin[1,2,3]

1. SANKEN, The University of Osaka, 8-1, Mihogaoka, Ibaraki, Osaka, 567-0047, Japan

2. Research Laboratory for Quantum Beam Science, SANKEN, The University of Osaka, 8-1, Mihogaoka, Ibaraki, Osaka, 567-0047, Japan

3. RIKEN SPring-8 Center, 1-1-1 Kohto, Sayo, Hyogo, 679-5148, Japan

4. Graduate School of Medicine, The University of Osaka, 1-7, Yamadaoka, Suita, Osaka, 565-0871, Japan

**Corresponding authors; hosokai@sanken.osaka-u.ac.jp (T. H.), yyamashita@sanken.osaka-u.ac.jp (Y. Y.)*

Abstract

Recent advances in laser wakefield acceleration (LWFA) have enabled well-defined beam conditions for quantitative studies of ultrashort electron beams in dense media. Here, using an LWFA electron-beam platform whose beam quality and transport capability were previously benchmarked through extreme-ultraviolet (XUV) free-electron-laser (FEL) amplification on the same beamline, we demonstrate that ultrashort electron beams can propagate through a 20 cm water target while retaining their ability to trigger depth-dependent chemical activation. Model substrate conversion closely followed the measured depth-dose distribution, indicating that the chemical response is primarily governed by local dose deposition even under ultrashort pulse conditions. While the overall depth-dose behavior was broadly consistent with conventional transport expectations, localized deviations were observed in the central beam region. Complementary experiments using a radio-frequency electron accelerator evaluated the underlying beam-induced reductive chemistry through model substrate conversion, functional prodrug activation, and subsequent cellular and in vivo responses. Together, these findings establish a proof-of-concept framework linking ultrashort LWFA electron-beam transport and energy deposition in deep aqueous media to beam-induced chemical activation and its functional biological consequences.

1. Introduction

Very-high-energy electron (VHEE) beams, referring to electron beams in the several-hundred-MeV energy range in the context of radiation therapy, have long been recognized for their favorable deep-penetration characteristics in biological tissue [1, 2]. Laser wakefield acceleration (LWFA), a plasma-based ultra-high-gradient acceleration technique that has long been investigated for its capability to generate ultrashort high-energy electron beams [3, 4], has also attracted growing interest as a compact source of VHEE beams for potential medical applications. A number of conceptual, dosimetric, and experimental studies, including Monte Carlo-based investigations [5, 6] and proof-of-principle irradiation experiments using biological targets [7, 8], have been reported. These pioneering studies demonstrated that the macroscopic dose deposition and biological responses of early-generation LWFA electron beams could largely be interpreted within conventional radiation transport frameworks. More recently, preclinical tumor irradiation using LWFA-based VHEE beams has also been reported [9].

While ionization of water by X-rays and high-energy charged particles generates reactive species that induce radiation chemical reactions in aqueous environments and contribute to indirect DNA damage in radiation therapy [10], such reactions can also be utilized for localized chemical transformations in aqueous environments. For example, hydrated electrons and other reactive species generated by irradiation modalities such as X-rays can induce reductive chemical reactions capable of activating chemically masked functional molecules, including prodrugs [11]. In thick aqueous media relevant to biological environments, such chemistry provides a potential framework in which high-energy electron beams function not only as sources of energy deposition but also as triggers for localized chemical activation.

Realization of such a concept using ultrashort LWFA electron beams requires reliable beam propagation through thick aqueous media while maintaining the capability for beam-induced chemistry at depth. In addition to their favorable penetration characteristics, ultrashort LWFA electron bunches possess extremely high particle density associated with their femtosecond-scale duration. Under such conditions, beam transport and energy deposition may not necessarily be described entirely by assumptions commonly applied to conventional electron beams. Recent theoretical studies have suggested that coherent stopping power effects could influence ultrashort electron bunch transport in water [12]. Previous Monte Carlo transport calculations have established the favorable deep-penetration characteristics of VHEE-class electron beams in dense media owing to their high beam energy [5]. These calculations generally model electron transport without explicitly considering the ultrashort temporal structure of LWFA electron bunches. Accordingly, they do not directly address the coupling between ultrashort beam propagation, energy deposition, and beam-induced chemistry in thick aqueous media. Experimental investigations of such coupled processes remain extremely limited, and their implications for quantitative chemical and biological responses have yet to be systematically examined. In recent years, however, substantial progress has been achieved in the generation and transport of high-quality LWFA electron beams [13, 14, 15]. Among these advances, the demonstration of XUV free-electron laser (FEL) amplification using LWFA electron beams [13,16] represents a particularly important technological milestone, providing a comprehensive benchmark of beam quality through the simultaneous control of multiple beam parameters, including pointing stability, beam energy stability, energy spread, charge stability, emittance, and ultrashort pulse duration [13]. Such technological maturity has begun to enable systematic experimental investigations of ultrashort beam–matter interaction regimes that were previously difficult to access.

Motivated by these developments, the present study investigates deep-water propagation and depth-dependent beam-induced chemistry using VHEE-class LWFA electron beams. To investigate the consequences of the underlying beam-induced reductive chemistry across multiple functional levels,

complementary radio-frequency (RF) linear accelerator–based chemical, cellular, and in vivo experimental platforms were also employed.

Here, we demonstrate that ultrashort VHEE-class LWFA electron beams can propagate through thick aqueous media while retaining their capability for beam-induced chemistry at depth. We further show that the functional consequences of the underlying beam-induced chemistry extend from localized chemical activation to measurable biological responses across multiple experimental platforms. These results provide experimental insight into the coupling between ultrashort beam propagation and beam-induced chemistry in deep aqueous media.

2. Experimental platforms and validation strategy

In the present study, we first experimentally investigated the propagation behavior and dose deposition characteristics of VHEE-class LWFA electron beams in thick aqueous media, and examined whether beam-induced chemical reactions could be achieved under deep-medium conditions. Furthermore, to evaluate whether the underlying beam-induced reductive chemistry could be progressively extended from localized chemical activation to cellular and in vivo biological responses, we employed purpose-designed electron beam experimental platforms based on both laser wakefield acceleration (LWFA) and a conventional L-band radio-frequency accelerator. Representative photographs of the experimental platforms and sample irradiation configurations used in the present study are shown in Supplementary Figure S1.

2. 1 LWFA platform for electron beam transport and model substrate activation in deep aqueous media

Electron beam transport and model substrate activation experiments in deep high-density media were performed using the LAPLACIAN (Laser Acceleration Platform as a Coordinated Innovative Anchor) facility installed at the RIKEN SPring-8 Center [17]. LAPLACIAN is a research platform for high-quality LWFA electron beams in the several-hundred-MeV to GeV energy range. Various key technologies for improving beam quality and stability [18,19], as well as advanced beam characterization studies [20], have been developed on this platform, demonstrating its capability for reproducible experimental investigations using high-quality ultrashort electron beams. More recently, the platform has successfully demonstrated XUV free-electron laser (FEL) amplification driven by LWFA electron beams [13], further establishing the maturity of stable and reproducible high-energy electron beam generation technologies. Importantly, the irradiation target in the present study was positioned immediately downstream from the undulator used for the FEL amplification experiments on the same beamline. Beam characterization studies performed during FEL operation confirmed transport of a highly localized electron beam through the undulator section to a position corresponding to the present water target [13], providing an experimentally validated benchmark for the beam quality delivered to the target after multi-metre propagation.

A schematic overview of the LWFA electron beam irradiation system used in the present study is shown in Figure 1(a). Beamline 2 of the Ti:sapphire femtosecond laser system installed at LAPLACIAN was employed. A high-intensity ultrashort-pulse laser with a central wavelength of 800 nm was focused onto a supersonic gas-jet target using a gold-coated off-axis parabolic mirror with a focal length of 1.5 m to drive LWFA. Shock injection [21] was adopted for electron injection, in which a sharp density transition formed within the supersonic gas jet enabled the generation of quasi-monoenergetic and highly stable several-hundred-MeV electron beams with sufficiently narrow energy spread to suppress substantial velocity-dispersion-induced temporal broadening during downstream transport. After characterization using beam monitors and an electron spectrometer in

the vacuum beamline, the generated electron beams were extracted into air through a 20-μm-thick titanium window and irradiated onto a 20-cm-thick water target positioned ~7 m downstream from the LWFA source (gas jet). This configuration enabled direct investigation of the deep propagation behavior and beam-induced chemical activation capability of ~370 MeV LWFA electron beams in dense media. Specifically, the deep propagation characteristics of the electron beam and the reduction reaction of a model substrate placed at defined depths within the 20-cm water target were evaluated simultaneously.

The depth-dependent dose deposition behavior during beam transport and the absorbed dose in the vial samples were evaluated using Gafchromic film (EBT-3, Ashland Co. Ltd.), which has been widely employed for high-dose-rate electron beam dosimetry [22], and potassium thiocyanate (KSCN) chemical dosimetry [23]. In particular, because LWFA electron beams possess an ultrashort femtosecond pulse structure, KSCN chemical dosimetry, which has recently been applied as a chemical dosimeter for ultrashort-pulse radiation fields in pulse radiolysis studies [24], was employed as an independent cross-check of the dose evaluation obtained using Gafchromic film, with transient absorption monitored using a 450 nm laser diode probe. The probe beam maintained an approximately elliptical cross section of 1.0 × 1.5 mm (FWHM, horizontal × vertical) throughout the KSCN measurement region, thereby sampling a localized region around the beam propagation axis.

To evaluate the feasibility of beam-induced reductive chemistry using LWFA electron beams, the azide-to-amine reduction reaction of model substrate azide **1** was employed as a representative model reaction in the present study.

2.2 Conventional L-band linear accelerator platform for chemical and functional validation

In the deep-water LWFA experiments, beam-induced chemical reactions under deep-medium conditions were evaluated using the azide-group reduction reaction of a model substrate as a representative indicator reaction. To further investigate whether this reductive chemical activation process could be extended to cellular and in vivo biological responses through activation of chemically masked anticancer compounds, additional chemical, cellular, and in vivo experiments were performed using relatively thin targets with thicknesses below 1 cm. In these experiments, the primary objective was not deep penetration into thick media, which requires several-hundred-MeV electron beams, but rather the evaluation of electron beam-induced chemical reactions and their associated biological responses. In addition, because the LWFA experimental platform used in the present study is subject to limitations in facility access time and available shot numbers, systematic chemical and biological evaluations over multiple dose conditions are not straightforward to perform efficiently.

Therefore, considering electron beam penetration capability, target thickness and size, sufficient irradiation shot numbers, and overall experimental efficiency, chemical and biological validation experiments were carried out using a conventional L-band radio-frequency (RF) electron linac (~30 MeV) installed at the Research Laboratory for Quantum Beam Science, Institute of Scientific and Industrial Research (SANKEN), the University of Osaka [25]. A schematic overview of the L-band RF electron beam irradiation system is shown in Figure 1(b). This accelerator is a conventional RF electron accelerator capable of providing stable ~30 MeV electron beams by accelerating thermionically generated electrons using 1.3 GHz L-band microwaves, and has been widely utilized for electron beam-induced chemistry studies and quantum beam research. The generated electron beam was extracted into air through a 20-μm-thick titanium window and irradiated onto target samples positioned ~20 cm downstream from the window. Representative beam conditions used in the present study were an electron energy of ~27 MeV at the target position, an energy spread below

3%, a pulse duration of ~8 ns, and a beam diameter of approximately 10 mm at the sample position. Dose evaluation was performed using Gafchromic film (EBT-3, Ashland Co. Ltd.) [22] and KSCN chemical dosimetry [23], consistent with the LWFA experiments, but with transient absorption monitored using a Xe flash lamp and spectrometer system.

Electron beams with energies of ~27 MeV provide sufficient penetration depth for relatively thin targets, including chemical samples contained in 1-cm-diameter plastic vials, cultured cancer cells, and cancer-model mouse tumors with thicknesses below approximately 1 cm. The propagation characteristics and depth–dose behavior of the 27 MeV electron beam in water-equivalent media were evaluated using Monte Carlo simulations performed with the Particle and Heavy Ion Transport code System (PHITS) [26]. Representative results are shown in Supplementary Figure S2, demonstrating effective beam penetration across the target geometries employed in the present chemical, cellular, and in vivo experiments. Detailed simulation conditions are described in Methods 2.

Utilizing this platform, the present study evaluated dose-dependent reduction reactions of model substrates, activation of chemically masked functional molecules, cellular responses associated with electron beam-induced chemical activation, and in vivo responses in cancer-model mice.

2. 2. 1 Reduction reaction of a model substrate and prodrug activation

In the present study, attention was focused on azide-group reduction reactions induced by hydrated electrons and hydrogen radicals generated in water during electron beam irradiation, and these reactions were regarded as a common fundamental reductive chemical mechanism underlying both model substrate reduction reaction and functional molecule activation. First, the electron beam-induced azide-to-amine reduction reaction of model substrate azide **1** was evaluated.

Next, as a representative example of a chemically masked functional molecule, activation of prodrug **3**, which was designed as a chemically masked form of the anticancer drug doxorubicin [11], was investigated. Doxorubicin is widely known as an anticancer agent used for various cancer types. Activation of the prodrug is initiated by azide-group reduction induced by reductive reactive species generated from water molecules during electron beam irradiation, followed by a 1,6-elimination reaction that releases active doxorubicin. Details of the prodrug design and activation mechanism are described in Methods 5.

Chemical reaction experiments were performed using 1-cm-diameter plastic vials as reaction containers. Compound concentrations were set to 10 μM considering the detection limit of the reaction products by ultra-performance liquid chromatography (UPLC) analysis. To ensure quantitatively detectable amounts of reaction products, electron beam irradiation doses of up to 60 Gy (1.0 Gy × 60 pulses at 0.1 Hz) for the model substrate experiments and up to 40 Gy (1.0 Gy × 40 pulses at 0.1 Hz) for the prodrug experiments were employed. These high-dose conditions substantially exceeded the maximum dose conditions of approximately 4 Gy used in the cellular and animal experiments, but were specifically selected for quantitative evaluation of the feasibility of chemical activation. In addition, to enhance the efficiency of the reductive reactions, dissolved oxygen concentrations in the sample solutions were reduced to below several μM by argon bubbling prior to irradiation. Detailed procedures for sample preparation and chemical analyses are described in Methods 6.

2. 2. 2 Cancer cell viability following prodrug activation

To evaluate whether electron beam-induced chemical activation could be detected as a cellular response in cultured cancer cells, in vitro cell experiments were subsequently performed. As a representative example, HeLa human cervical cancer cells were used to evaluate cellular responses following electron beam irradiation of prodrug **3**. HeLa cells were seeded onto collagen-coated 1-cm-diameter plastic vials at an initial density of 3,000 cells/vial (150 μL/vial) and cultured at 37 °C for 24 h. Subsequently, the culture medium was removed, and prodrug **3** diluted in DMEM (30 nM) was added. The cells were then treated under conditions of prodrug alone, electron beam irradiation alone, or combined treatment. In experiments using the L-band RF electron linac, electron beam irradiation was performed at a total dose of 4.4 Gy (1.1 Gy/pulse × 4 pulses at 0.1 Hz). Following electron beam irradiation, the cells were cultured for 72 h at 37 °C under 5% CO_2 conditions. The culture medium was then removed, and Alamar Blue™ solution (10 μL in 100 μL medium) was added and allowed to react for 3 h. Cell viability was subsequently evaluated using a fluorescence microplate reader (EnSight™, PerkinElmer; excitation 540 nm, emission 590 nm). Detailed procedures for cell viability assays are described in Methods 7.

2.2.3 In vivo responses following beam-induced chemical activation

To evaluate whether electron beam-induced chemical activation could be detected as a functional response in vivo, animal experiments were performed using a mouse model of cancer. In the present study, to clearly define the electron beam irradiation conditions and minimize unnecessary radiation exposure to surrounding organs, a subcutaneous tumor model formed in the rear limb was employed rather than an orthotopic transplantation model. In each mouse (female BALB/c nude mice, 6 weeks old), HeLa cells (1.0 × 10^6 cells) were subcutaneously transplanted into the right rear limb. Four weeks after transplantation, in vivo response evaluations were performed under conditions in which the tumor thickness remained below 1 cm.

Mice were divided into four groups: control (CTRL), prodrug **3** alone (1.0 mg/kg), electron beam irradiation alone (4.0 Gy total dose; 1.0 Gy/pulse × 4 pulses at 0.1 Hz), and combined prodrug **3** plus electron beam irradiation (Prodrug+EB). Prodrug **3** or vehicle was administered subcutaneously 4 h before electron beam irradiation. Thirty-one days after irradiation, the mice were euthanized, and antitumor effects were evaluated using excised tumor weight as the primary endpoint.
Detailed procedures for the in vivo therapeutic study, histopathological safety assessments, and histological processing and staining are described in Methods 8–10. For safety evaluation, normal muscle tissues adjacent to the tumor were also collected, and the effects of electron beam irradiation on normal tissues were evaluated histopathologically.

3. Results

3.1 Characterization of the LWFA platform

First, the beam stability and reproducibility of the LWFA platform employed for the deep-water interaction experiments were characterized. The generated electron beam exhibited a central energy of approximately 370 MeV, a narrow energy spread of ~0.8% (rms), approaching the resolution limit of the electron spectrometer, and an average beam charge of ~18.5 pC. In addition, a pointing stability of ~0.17 mrad was achieved, indicating stable beam transport suitable for downstream interaction experiments. The electron bunch duration was estimated to be in the few-femtosecond regime based on particle-in-cell (PIC) simulations [27]. This estimate was further supported by FEL simulations

performed using the SIMPLEX code [28], which successfully reproduced the experimentally observed XUV FEL amplification on the same beamline [13]. Together with the FEL amplification benchmark previously demonstrated on the same beamline, these characteristics support delivery of an ultrashort high-quality electron beam to the downstream irradiation position. The combination of femtosecond bunch duration, stable transport characteristics, and FEL-compatible beam quality places the present beam parameters in a regime relevant to ultrashort beam–matter interaction studies beyond those typically encountered in conventional accelerator-based electron-beam irradiation [12, 29].

The shot-to-shot stability of the beam was further evaluated, as summarized in Figure 2. The beam centroid positions measured using the S1 phosphor-screen monitor (Figure 1a), located approximately 1 m downstream from the LWFA source, remained stable over 50 consecutive shots (Figure 2a). The beam charge was also consistently maintained over the same 50-shot sequence (Figure 2b), confirming reproducible charge delivery for subsequent dosimetric and chemical analyses. In addition, the central beam energy remained highly stable throughout the measurement sequence (Figure 2c), while the corresponding electron energy spectra exhibited reproducible quasi-monoenergetic features with a narrow energy spread (Figure 2d). These results confirm stable generation of high-quality LWFA electron beams for the deep-water interaction experiments. In addition to the source-point stability shown in Figure 2, beam-profile measurements performed at the S3 and S4 phosphor-screen monitors (Figure 1a) during FEL operation demonstrated transport of a highly localized electron beam through the undulator section and up to a position corresponding to the downstream end of the present water target [13]. These measurements showed beam sizes below approximately 200 μm (FWHM) at both locations together with near-parallel propagation, confirming preservation of FEL-compatible beam quality over approximately 8 m of transport from the LWFA source.

Consistent beam delivery under the deep-water experimental configuration was further confirmed by accumulated irradiation profile measurements obtained at the water-target entrance (~7 m downstream from the LWFA source) using Gafchromic films (Supplementary Figure S3). These measurements confirmed reproducible beam delivery to the target location. Although the observed irradiation field was broader than the intrinsic beam size measured using phosphor-screen diagnostics, reflecting the effects of beam extraction and subsequent propagation, the accumulated beam profile remained well localized at the water-target entrance.

3.2 Deep-water propagation and model substrate activation using LWFA electrons

Using the stable and high-quality LWFA electron beam platform characterized in Section 3.1, deep beam transport and beam-induced reductive chemistry were investigated in a 20 cm-thick water target by correlating electron beam propagation behavior with reduction reaction of the model substrate azide **1** positioned at defined depths within the target. As shown in Figure 3a and 3b, the ~370 MeV LWFA electron beam deposited measurable dose throughout the 20 cm-thick water target. Dose deposition remained detectable over the entire target length, confirming that the LWFA electron beam retained its ability to transport energy to substantial depths within dense aqueous media. The corresponding evolution of the beam diameter during propagation is summarized in Figure 3c. As expected from multiple scattering in water, the beam gradually broadened with increasing propagation depth while remaining clearly identifiable throughout the target. Representative examples of the 10-shot accumulated Gafchromic film images used for the depth-dose analysis are shown in Supplementary Figure S1a.

For comparison, Monte Carlo simulations of electron beam transport in water were performed using the experimentally measured beam energy, beam charge, beam size, and divergence as input parameters. The calculated normalized depth-dose distributions are shown together with the experimental results in Figure 3a and 3b, while the calculated beam transport behavior is compared with the measured spot evolution in Figure 3c. The overall depth-dependent dose profile obtained using the 10 mm integration diameter showed broad agreement with the Monte Carlo prediction. In contrast, the central 200 μm analysis region exhibited a modest deviation from the calculated profile in the shallow-to-intermediate depth region. These observations indicate that the overall beam transport behavior is largely described by conventional electron transport calculations, while the most localized component of the transported beam may exhibit behavior not fully captured by the broader profile analysis. Details of the Monte Carlo calculations are provided in Methods 2.

Furthermore, as shown in Figure 3d, depth-dependent azide-to-amine reduction of the model substrate was observed throughout the water target. Model substrate conversion measurements were performed at the same defined depths used for the Gafchromic film dosimetry analysis. The chemical conversion profile broadly followed the depth-dependent behavior of the overall beam transport shown in Figure 3b, indicating that beam-triggered reductive chemistry remained inducible after deep-water propagation of the LWFA electron beam. Independent dose evaluation using a KSCN chemical dosimeter based on pulse radiolysis showed quantitative agreement with the Gafchromic film measurements within the overlapping depth region of 5–13 cm (Supplementary Figure S4), supporting the validity of the depth-dose distributions obtained under the present experimental conditions. Together, these results indicate that beam-triggered chemical activation in deep aqueous media is closely linked to local energy deposition and demonstrate that ultrashort LWFA electron beams can retain their capability to induce reductive chemistry even after propagation through 20 cm of water.

3.3 Chemical validation of model substrate reduction reaction and prodrug activation using the conventional RF platform

In the previous section, we demonstrated that ultrashort LWFA electron beams retain their capability to induce azide reduction of the model substrate even after deep-water propagation. To quantitatively characterize the underlying beam-induced reductive chemistry under highly controlled and reproducible irradiation conditions, the reduction reaction of the model substrate azide **1** was further investigated in detail using the complementary RF linac platform.

Reduction reaction of the model compound azide **1** to amine **2** under electron beam irradiation was first investigated as a representative beam-induced reductive reaction (Figure 4a). Electron beam irradiation at a dose of 60 Gy converted azide **1** to amine **2** with a yield of 28% (Figure 4b). Furthermore, the conversion of azide **1** to amine **2** increased with irradiation dose up to approximately 60 Gy, demonstrating a clear dose-dependent behavior (Figure 4c). This result establishes the dose-governed nature of the key reductive reaction underlying prodrug activation.

Subsequently, activation of the chemically masked doxorubicin prodrug **3** by electron beam irradiation was investigated. As schematically illustrated in Figure 5a, electron beam irradiation induces reductive activation of the chemically masked doxorubicin prodrug through azide reduction, leading to release of the active anticancer agent doxorubicin. Irradiation of prodrug **3** (10 μM) with electron beams (40 Gy) yielded doxorubicin with a yield of 15% (Figure 5b). The activation proceeds via a sequence of reactions (Supplementary Figure S5): electron beam irradiation generates hydrated electrons and hydrogen radicals from water molecules, which reduce the azide group to form an amine intermediate, followed by spontaneous mask cleavage and decarboxylation to release the active drug.

These results demonstrate beam-induced activation of phenylazide-masked doxorubicin prodrug in aqueous solution.

Using the conventional RF platform, the chemical behavior of the model reduction reaction was quantitatively characterized, including its dose dependence and reproducibility. These results establish the reduction reaction as a key beam-induced chemical process and provide a mechanistic basis for interpreting the beam-triggered chemical activation observed in the LWFA deep-water experiments. All results described above were obtained under the common experimental conditions described in Section 2.2.1. The relatively high compound concentrations and irradiation doses were employed to ensure reliable detection of chemical products by UPLC and quantitative evaluation of beam-induced chemical conversion. Reduction reaction efficiency was further enhanced by decreasing dissolved oxygen concentration through argon bubbling.

3.4 In vitro cellular responses following RF beam-induced chemical activation

Cell viability was evaluated after 72-hour incubation to assess whether electron beam–induced chemical activation could produce measurable cellular responses, following the experimental workflow shown in Figure 6a and described in Section 2.2.2. As shown in Figure 6b, no significant difference in cell viability was observed between the control group (CTRL) and the group treated with prodrug **3** alone (Prodrug). Electron beam irradiation alone at a total dose of 4.4 Gy (1.1 Gy/pulse × 4 pulses at 0.1 Hz) using the L-band linear accelerator (EB) induced moderate cytotoxicity, reducing cancer cell viability by approximately 30%. In contrast, the combination treatment (Prodrug+EB) induced an additional cytotoxic effect exceeding 20%, resulting in an overall reduction in cancer cell viability of approximately 50%. These results indicate that electron beam (EB) irradiation is independently cytotoxic and that the combined Prodrug+EB treatment further enhances the reduction in cancer cell viability.

3.5 In vivo biological responses following RF beam-induced chemical activation

Tumor-bearing mice were divided into four treatment groups: control (CTRL), prodrug **3** alone (Prodrug), electron beam irradiation alone (EB), and combined treatment (Prodrug+EB), as shown in Figure 7a. Electron beam irradiation was performed at a total dose of 4 Gy. Tumor weight outcomes across the four treatment groups are presented in Figure 7b. No significant difference in tumor weight was observed between the control group (CTRL) and the group treated with prodrug **3** alone (Prodrug), indicating negligible antitumor activity of the prodrug in the absence of irradiation. Electron beam irradiation alone (EB) produced moderate tumor suppression, resulting in an approximately 25% reduction in tumor weight relative to the control group. In contrast, the combination treatment (Prodrug+EB) produced the largest reduction in tumor weight (~54%) among the four groups and yielded a significantly greater response compared to electron beam irradiation alone (EB) ($P < 0.05$; Tukey's test; * in Figure 7b). These results indicate that electron beam irradiation enhances the biological response associated with activation of prodrug **3**. This enhanced response is consistent with the in vitro cell viability results and is also consistent with irradiation-induced activation of prodrug **3** in vivo. Overall, these findings demonstrate that electron beam–triggered chemical activation produces a measurable in vivo biological response in a mouse model of cancer. Detailed statistical analyses and significance criteria are described in Methods 11.

In addition, histological analysis was performed to assess whether electron beam irradiation induced tissue damage. In the in vivo tumor model, muscle tissue adjacent to the tumor in the rear limb was harvested at the time of tumor excision, four weeks after irradiation with a 4 Gy electron beam. No significant histomorphological changes attributable to electron beam irradiation were observed in the

muscle tissue adjacent to the tumor, indicating minimal tissue impairment. Representative histological images are shown in Supplementary Figure S6. Detailed experimental procedures for the in vivo study and histopathological safety assessment, including tissue processing and staining protocols, are provided in Methods 8–10.

4. Discussion

The present study demonstrates that ultrashort, high-density electron beams generated by laser wakefield acceleration (LWFA) can propagate through deep aqueous media and induce beam-triggered chemical activation. Complementary experiments using a conventional RF linear accelerator establish the generality and functional relevance of the underlying reaction mechanism, enabling its systematic validation across chemical, cellular, and in vivo systems.

To interpret the physical significance of these observations, the relationship between depth-dependent dose deposition measured using Gafchromic film and model substrate conversion was examined. The close correspondence between the measured normalized depth-dose profile and model substrate conversion indicates that, under the present experimental conditions, the chemical response in deep aqueous media is primarily governed by depth-dependent dose deposition. Notably, this dose-governed behavior persists even under ultrashort pulse conditions in the few-femtosecond regime characteristic of LWFA electron beams. While ultrashort, high-density electron beams are expected to exhibit distinct ionization dynamics, potentially involving coherent or collective effects [12, 29], the present results suggest that such effects do not dominate the overall chemical response under the conditions investigated here. The close agreement between film-derived normalized depth-dose profiles and independently measured depth-dependent chemical conversion further argues against major distortion of the Gafchromic film response under the present conditions. In addition, independent dose measurements using a pulse-radiolysis-based KSCN chemical dosimeter over the overlapping depth region (5–13 cm) yielded quantitatively consistent dose levels with the Gafchromic film measurements (Supplementary Figure S4). This consistency further supports the validity of the depth-dependent dose profile obtained from the film measurements under the present ultrashort LWFA irradiation conditions. Monte Carlo calculations for the 27 MeV electron beam used in the RF accelerator experiments demonstrated sufficient penetration through the representative target geometries employed in the chemical and biological studies (Supplementary Figure S2), supporting the use of the RF platform for systematic validation experiments.

In contrast, comparison with Monte Carlo simulations revealed a more nuanced picture. While the overall normalized depth-dose distribution integrated over the full beam profile showed broad agreement with the corresponding Monte Carlo prediction for a conventional ~370 MeV electron beam (Figure 3b), localized deviations became more apparent when the analysis was restricted to the central beam region (Figure 3a). This observation suggests that any discrepancy between experiment and simulation is concentrated within a limited portion of the beam profile rather than being representative of the overall energy-deposition behavior. In the central 200 μm analysis region, the measured profile exhibited a modest deviation from the conventional Monte Carlo prediction in the shallow-to-intermediate depth region, whereas the broader 10 mm integration region followed the calculated overall transport behavior more closely. Because the beam diameter increased substantially with propagation depth, determination of the beam center becomes progressively more sensitive at larger depths, and therefore the central-region values should be interpreted with appropriate caution. Nevertheless, the comparison suggests that the most localized component of the transported LWFA beam may exhibit behavior that is partially averaged out when the analysis is extended to the full beam profile. The physical origin of this localized behavior remains to be clarified.

The localized deviation observed in the central beam region is particularly noteworthy. In the present LWFA platform, successful XUV FEL amplification on the same beamline provides an experimentally validated benchmark indicating preservation of ultrashort beam quality after multi-metre transport. In addition, beam-profile measurements performed at the S3 and S4 phosphor-screen monitors demonstrated transport of a highly localized beam with a diameter below approximately 200 μm (FWHM) over approximately 8 m from the LWFA source. Together with the few-femtosecond bunch duration estimated from PIC and FEL simulations, these characteristics place the present beam parameters within the regime discussed in recent theoretical studies of collective or coherent energy-deposition effects in ultrashort electron bunch irradiation [12, 29]. Previous theoretical studies have suggested that collective or coherent energy-deposition effects may become relevant at beam densities on the order of 10^15 cm^−3 [12]. Although the present study does not provide direct evidence for such effects, an order-of-magnitude estimate based on beam parameters validated through the FEL amplification study [13] suggests that a highly localized high-density beam core within the transported LWFA beam may approach this density scale.

While the overall dose deposition and chemical activation behavior remained broadly consistent with conventional dose-governed expectations, the localized deviation observed in the central beam region suggests that beam–matter interaction processes within a limited portion of the beam profile may not be fully captured by conventional transport models. Further investigation will be required to determine whether this behavior is associated with localized high-density beam components, coherent energy-deposition effects, or other ultrashort beam–matter interaction mechanisms.

Earlier LWFA irradiation studies generally reported macroscopic dose deposition and biological responses broadly comparable to those obtained using conventional accelerator-based electron beams [6, 7, 8]. However, in many previous studies, direct experimental validation of beam quality at the downstream interaction region remained limited, and irradiation targets were often positioned relatively close to the LWFA source to minimize possible degradation of the ultrashort beam structure during transport. In the present platform, stable beam transport over approximately 8 m, together with experimentally demonstrated XUV FEL amplification and sub-200 μm beam sizes measured at downstream beam monitors, provides a unique benchmark supporting delivery of a well-defined ultrashort beam to the interaction region. Within this experimentally validated ultrashort interaction regime, the present study demonstrates that LWFA electron beams can induce beam-triggered chemical activation after propagation through deep aqueous media.

To assess the generality of the dose-governed chemical activation behavior beyond the specific LWFA conditions, complementary experiments were performed using a conventional RF linear accelerator. This platform enabled systematic evaluation of the underlying reduction-reaction chemistry under highly reproducible irradiation conditions, including quantitative characterization of dose dependence and prodrug activation efficiency. The results confirmed that the observed dose-governed activation pathway is not unique to LWFA but instead reflects a generalizable mechanism of electron beam–induced chemical activation. These complementary measurements provide a mechanistic framework for interpreting the beam-triggered chemical activation observed in the LWFA deep-water experiments.

Beyond the physical transport and chemical activation processes discussed above, the present results demonstrate that beam-triggered chemical activation can be extended across multiple functional levels, from model chemical reactions to functional prodrug activation and measurable biological responses in cellular and in vivo systems. Even under normoxic cellular conditions, where dissolved oxygen competitively suppresses hydrated-electron reactions, measurable biological responses associated with beam-induced prodrug activation were observed. These observations suggest that oxygen concentration may influence the efficiency of beam-triggered reductive activation under biologically relevant conditions and motivate further investigation of oxygen-dependent activation behavior. These findings indicate that the underlying beam-induced chemical processes identified

here can provide a functional link between ultrashort beam transport, local energy deposition, chemical activation, and subsequent biological responses. While radiation-induced prodrug activation has previously been reported using other irradiation modalities such as X-rays [11], the present RF experiments demonstrate electron-beam-triggered prodrug activation, while the LWFA experiments establish that the underlying reductive chemistry remains inducible following deep-water propagation of ultrashort high-energy electron beams. A conceptual framework illustrating this multiscale coupling—from ultrashort beam transport and energy deposition to localized chemical activation and subsequent biological response—is presented in Figure 8. The schematic is intended to summarize the physical and chemical principles demonstrated in the present study rather than depict a clinical implementation.

To further elucidate the relationship between ultrashort beam transport, local energy deposition, chemical activation, and biological response, additional experimental and theoretical investigations will be required. Such studies may provide deeper insight into beam–matter interactions in dense media and their potential functional consequences. From a system-level perspective, the framework identified in this study may be extended toward integrated irradiation platforms based on laser-driven electron sources such as LWFA. A schematic representation of a potential beam-delivery configuration, illustrating the coupling of laser-driven acceleration and beam transport to a target, is provided in Supplementary Figure S7 for illustrative purposes. In such a framework, high-energy electron beams can serve not only as agents of energy deposition but also as triggers of localized chemical transformations within irradiated media. This perspective suggests the possibility of extending the role of radiation beyond conventional dose-delivery paradigms toward the controlled induction of localized chemical processes.

Conclusion

We have demonstrated that laser-wakefield-accelerated electron beams can propagate through deep aqueous media while retaining their ability to induce depth-dependent chemical activation. The observed correlation between depth-dependent dose deposition and chemical conversion indicates that the reaction behavior is primarily governed by the local dose distribution under the present experimental conditions. While the overall chemical response remained broadly consistent with dose-governed expectations, localized deviations from conventional transport predictions were observed in the central beam region. These results provide experimental evidence for a regime in which ultrashort, high-energy electron beams can be directly coupled to beam-induced chemical processes in dense media. The functional consequences of the underlying beam-induced chemistry were further demonstrated across multiple levels, from model chemical reactions to functional prodrug activation and measurable biological responses in cellular and in vivo systems. Together, these findings establish a proof-of-concept framework connecting ultrashort electron-beam transport and energy deposition in deep aqueous media with beam-induced chemical activation and its functional biological consequences.

Methods

1. Photographs of the sample irradiation configurations

Representative photographs of the experimental platforms used in the present study are shown in Supplementary Figure S1. The photographs illustrate the actual irradiation geometries employed for the LWFA deep-water propagation experiments and the conventional L-band RF electron linac studies. For the LWFA deep-water experiments, representative examples of 10-shot accumulated

Gafchromic film images obtained at selected depths are also shown to illustrate the beam-profile measurements underlying the depth-dose and beam-transport analyses presented in Figure 3.

2. Monte Carlo simulation of conventional electron beam transport in water

Conventional 370 MeV electron beam calculations

Monte Carlo simulations were performed to calculate the depth–dose distributions of conventional electron beams propagating through water targets as a reference for comparison with the experimentally measured LWFA depth-dependent dose distributions. The simulations were carried out using the Particle and Heavy Ion Transport code System (PHITS) [26] under geometrical conditions corresponding to the experimental configurations used in the present study. The calculation did not incorporate the femtosecond temporal structure or the high instantaneous charge density characteristic of the LWFA electron beam.

For the LWFA comparison calculations, electron transport through the downstream air path following the titanium exit window and subsequent propagation within the 20 cm water target were simulated. The target geometry and detector positions corresponded to those used for the Gafchromic film measurements shown in Figure 1a. The entrance surface of the water target was positioned approximately 12.5 cm downstream from the titanium exit window, corresponding to the experimental irradiation configuration. The experimentally measured in-air beam parameters were used as input conditions for the simulations. The central beam energy was approximately 370 MeV, with a total charge of approximately 20 pC. The transverse beam profile at the water-target position was approximated by a Gaussian distribution using the measured beam dimensions, and the effective angular spread was determined from beam-profile measurements in air.

27 MeV L-band electron beam calculations

Monte Carlo calculations were performed for the approximately 27 MeV electron beam used in the chemical, cellular, and mouse irradiation experiments conducted with the conventional L-band RF electron linac. The simulation geometry incorporated the representative irradiation configurations employed in these experiments, including sample containers and water-equivalent target regions.

The simulations were used to evaluate the penetration characteristics and depth–dose behavior of the electron beam in water-equivalent media corresponding to the experimental sample geometries. As shown in Supplementary Figure S2, the calculated results indicated that the 27 MeV electron beam provided sufficient penetration depth for irradiation of all experimental targets used in this study, including 1 cm-diameter sample vials, cultured cancer cells, and mouse tumor models with characteristic thicknesses below approximately 1 cm.

3. LWFA beam transport stability

Representative Gafchromic film images obtained at the entrance of the water target during the deep-water propagation experiments were analyzed to evaluate the spatial localization of the transported LWFA beam. Supplementary Figure S3 shows a representative beam spot image accumulated over ten consecutive LWFA shots together with the corresponding lateral beam profile. A compact and localized irradiation pattern remained clearly observable after multi-shot accumulation, indicating reproducible beam delivery to the water-target entrance under the present experimental conditions. The corresponding lateral beam profile exhibited an apparent full width at half maximum (FWHM)

of approximately 690 μm. Because the accumulated profile was obtained from multiple LWFA shots, the measured width should be regarded as an approximate indication of the effective irradiation-field size at the water-target entrance rather than a precise determination of the intrinsic single-shot beam profile. The apparent beam size observed on the Gafchromic film was larger than that measured using the phosphor-screen monitors. This difference likely reflects the cumulative effects of shot-to-shot beam-position fluctuations during the ten-shot accumulation, together with contributions from scattered electrons and secondary radiation generated during transport through the titanium exit window and air path. Therefore, the observed profile represents the effective irradiation field delivered to the water-target entrance rather than the intrinsic single-shot LWFA beam size.

4. Independent validation of Gafchromic film dose measurements using KSCN chemical dosimetry

To further evaluate the validity of the Gafchromic film–based dose measurements under the present ultrashort, high-density LWFA electron beam conditions, independent dose measurements were performed using a pulse-radiolysis-based KSCN chemical dosimeter over representative depth regions within the water target. KSCN dosimetry was performed using four 2-cm optical-path-length quartz cells positioned sequentially along the beam axis. Gafchromic films were simultaneously placed at the entrance and exit surfaces of the quartz-cell assembly, corresponding to representative depth positions of 5, 7, 9, 11, and 15 cm within the water target. This configuration enabled comparison of the overall dose levels obtained by KSCN dosimetry with the depth-dependent dose profile measured using the films. The KSCN dose values represent the average over 10 LWFA shots, whereas the Gafchromic film dose values were obtained from films accumulated over 10 shots and normalized to the average dose per shot. Transient absorption measurements for the LWFA KSCN dosimetry were performed using a 450 nm laser diode probe, consistent with the LWFA pulse-radiolysis configuration described in the main text, whereas the RF accelerator experiments employed a Xe flash lamp and spectrometer system. The laser diode probe beam maintained an approximately elliptical profile with FWHM dimensions of 1.0 × 1.5 mm (horizontal × vertical) throughout the KSCN measurement region. For comparison with the KSCN measurements, Gafchromic film dose values were evaluated from a localized analysis region around the beam propagation axis, corresponding approximately to the region sampled by the laser diode probe beam.

5. Reaction scheme for electron beam-triggered activation of prodrug 3

A schematic reaction scheme for electron beam-triggered activation of prodrug **3** is shown in Supplementary Figure S5. Electron beam irradiation induces water radiolysis, generating reductive species that convert the azide group into an amine intermediate, followed by spontaneous release of the active drug.

6. Sample preparation and chemical analysis

Prodrugs and their corresponding model compounds were dissolved in DMSO to prepare 10 mM stock solutions, which were subsequently diluted in Milli-Q water or phosphate-buffered saline (PBS) to yield a final concentration of 10 μM in plastic vials. The solutions were degassed by bubbling argon gas through them for 10 minutes. The reaction induced by electron beam irradiation was monitored and analyzed by injecting the sample into an ACQUITY UPLC BEH C18 column (Waters, 186002350) at a flow rate of 1.0 mL/min, with UV detection at 254 nm (λ = 254 nm). The UPLC conditions were as follows: eluent A, water containing 0.1% formic acid; eluent B, acetonitrile

containing 0.1% formic acid. The gradient for eluent B was set as follows: 0–1 min, 1%; 1–17 min, 1–99%; 17–19 min, 99%; 19–20 min, 99–1%. The retention times—defined as the duration each compound remained on the column after injection—were as follows: azide **1**, 4.45 min; amine **2**, 2.08 min; prodrug **3**, 6.09 min; doxorubicin, 3.81 min. These retention times were determined using individually injected pure compounds.

7. Cell viability after electron beam irradiation

HeLa cells were seeded into plastic vials pre-coated with collagen in acetic acid (AcOH) at an initial density of 3000 cells per vial (150 μL per vial) and incubated at 37 °C for 24 hours. After removing the culture medium using an aspirator, prodrugs diluted in DMEM were added (150 μL per vial), and the vials were irradiated with electron beams at various dose levels. The cells were then incubated at 37 °C for 72 hours in a humidified atmosphere containing 5% CO_2 in air. After removing the medium using an aspirator, Alamar Blue™ solution (10 μL in 100 μL of medium) was added to each vial. The cells were incubated again at 37 °C for 3 hours. Fluorescence in each vial was measured using an EnSight™ multilabel reader (PerkinElmer, Inc.; excitation wavelength: 540 nm; emission wavelength: 590 nm). HeLa cells (JCRB9004) were obtained from the JCRB Cell Bank, National Institutes of Biomedical Innovation, Health and Nutrition, Osaka, Japan. As this study used an established and generally available cell line and did not involve human participants or newly collected human-derived specimens, approval by a human research ethics committee and informed consent were not required.

8. In vivo response study in a mouse model of cancer

All animal procedures were approved by the Animal Experiment Committee of the University of Osaka (Approval No. R04-1-0) and were performed in accordance with the relevant institutional and national guidelines and regulations. Female BALB/c nude mice (6 weeks old; Nihon-Clea, Tokyo, Japan) were housed under standard conditions with free access to food and water. Each mouse was inoculated subcutaneously with 1.0×10^6 HeLa cells into the right rear limb. Four weeks after tumor inoculation, tumor-bearing mice were randomly assigned to four treatment groups: control (CTRL), prodrug **3** alone (1.0 mg/kg; Prodrug), electron beam irradiation alone (EB), and prodrug **3** combined with electron beam irradiation (1.0 mg/kg; Prodrug+EB).

Prodrug **3** or vehicle was administered subcutaneously 4 hours prior to irradiation. Electron beam irradiation was performed using the L-band RF linear accelerator at a total dose of 4.0 Gy (1.0 Gy/pulse × 4 pulses at 0.1 Hz). Mice were euthanized on day 31 after irradiation by inhalation of sevoflurane (>5%). Excised tumors were weighed using a precision balance. Normal muscle tissues adjacent to the tumors were also collected for histopathological analysis.

9. Histopathological safety assessment following electron beam irradiation

To evaluate potential tissue damage induced by electron beam irradiation, muscle tissue adjacent to the tumor in the rear limb was harvested at the time of tumor excision, four weeks after irradiation with a 4 Gy electron beam, and subjected to histopathological analysis. Representative histological images of normal tissues adjacent to tumors are shown in Supplementary Figure S6.

10. Histological processing and staining

Harvested tissues were fixed in 10% neutral buffered formalin (Cat. #35057, Muto Pure Chemicals Co., Ltd., Japan) and rinsed with distilled water prior to processing. Ethanol dehydration and paraffin infiltration were performed using a spin tissue processor (STP120-3, MICROM, Germany). Samples were embedded in paraffin using an embedding system (EC350, MICROM, Germany), sectioned into 4 μm-thick slices using a sliding microtome (SM2000R, Leica Microsystems, Germany), and mounted onto glass slides (Cat. #S1112, Matsunami Glass Ind., Ltd., Japan). Sections were stained with hematoxylin and eosin (H&E), and images were acquired at 40× magnification using a microscope (BZ-X800L, Keyence Corporation, Japan).

11. Statistical analyses

All quantitative data are presented as mean ±standard deviation (s.d.). Statistical comparisons among three or more groups, or between two groups where appropriate, were performed using two-way analysis of variance (ANOVA) followed by Tukey's post hoc test for unpaired data. P values < 0.05 were considered statistically significant.

12. Conceptual LWFA-based beam delivery system

A conceptual illustration of a potential LWFA-based beam delivery system is shown in Supplementary Figure S7. The schematic presents a possible compact configuration for generating and transporting ultrashort high-energy electron beams using laser wakefield acceleration. The illustration is intended solely to provide a conceptual system-level perspective and does not represent a clinical or fully engineered implementation.

Acknowledgments

This work was supported by the JST-MIRAI Program (Grant No. JPMJMI17A1). The authors thank Drs. K. Huang, N. Nakanii, I. Daito, and M. Kando (KPSI, QST); Drs. S. Nishi and Y. Honda, A. Zhidkov, Mr. K. Furukawa, Mr. H. Kato, Ms. M. Izuhara, and Ms. Y. Hayashi (SANKEN, the University of Osaka); and SMARTSHELL Co., Ltd. for valuable discussions and technical support. The authors also acknowledge Prof. Y. Sano, Program Manager of the JST-MIRAI Program, and Dr. T. Ishikawa, Director of the RIKEN SPring-8 Center, for their support in the establishment of the LAPLACIAN facility under the ImPACT program of the Council for Science, Technology and Innovation (Cabinet Office, Government of Japan).

Author contributions

T.H. conceived the idea, designed the research strategy, led the project, performed the beam experiments, and wrote the manuscript. Y.Y. led the chemical studies, selected and prepared the chemical materials, directed the chemical analysis, and contributed to preparation of the chemistry- and cell experiment–related sections of the manuscript. Y.Miz. contributed to preparation of the sample targets and analysis of the beam-experiment data. K.N. and J.Y. contributed to the beam experiments. Y.Mur. contributed from a radiation chemistry perspective and provided conceptual input to the study. Z.J. played a central role in the development and long-term optimization of the

high-quality and stable LWFA beam platform that enabled the present study and participated in the LWFA experiments. K.Nak. contributed to the cell and in vivo experiments, and K.M. contributed to the in vivo experiments and preparation of the corresponding sections of the manuscript. T.M. and Y.-J.G. performed the Monte Carlo and PIC simulations. M.Ko. and Y.T. contributed from a radiation oncology perspective. T.S. provided guidance from organic chemistry and drug-discovery perspectives and supported the interdisciplinary collaboration underlying this study. All authors discussed the results and commented on the manuscript.

Data Availability

The datasets generated and/or analysed during the current study are available from the corresponding author on reasonable request.

Competing interests

The authors declare no competing interests.

References

[1] DesRosiers, C., Moskvin, V., Bielajew, A. F. & Papiez, L. 150-250 MeV electron beams in radiation therapy. *Phys. Med. Biol.* **45**, 1781-1805 (2000).

[2] Ronga, M. G. et al. Back to the future: very high-energy electrons (VHEEs) and their potential application in radiation therapy. *Cancers* **13**, 4942 (2021).

[3] Esarey, E., Schroeder, C. B. & Leemans, W. P. Physics of laser-driven plasma-based electron accelerators. *Rev. Mod. Phys.* **81**, 1229-1285 (2009).

[4] Hooker, S. M. Developments in laser-driven plasma accelerators. *Nat. Photonics* **7**, 775-782 (2013).

[5] Fuchs, T. et al. Treatment planning for laser-accelerated very-high energy electrons. *Phys. Med. Biol.* **54**, 3315-3328 (2009).

[6] Lundh, O. et al. Comparison of measured with calculated dose distribution from a 120-MeV electron beam from a laser-plasma accelerator. *Med. Phys.* **39**, 3501-3508 (2012).

[7] Laschinsky, L. et al. Radiobiological effectiveness of laser accelerated electrons in comparison to electron beams from a conventional linear accelerator. *J. Radiat. Res.* **53**, 395-403 (2012).

[8] Oppelt, M. et al. Comparison study of in vivo dose response to laser-driven versus conventional electron beam. *Radiat. Environ. Biophys.* **54**, 155-166 (2015).

[9] Guo, Z. et al. Preclinical tumor control with a laser-accelerated high-energy electron radiotherapy prototype. *Nat. Commun.* **16**, 1895 (2025).

[10] Hall, E. J. & Giaccia, A. J. *Radiobiology for the Radiologist.* 8th ed. (Lippincott Williams & Wilkins, 2018).

[11] Geng, J. et al. Switching on prodrugs using radiotherapy. *Nat. Chem.* **13**, 805-810 (2021).

[12] Curcio, A. et al. Dose increment in ultrashort particle irradiations via coherent stopping power. *Phys. Rev. Res.* **6**, 033334 (2024).

[13] Jin, Z. et al. Optimized laser wakefield acceleration: generating stable, high-energy, monoenergetic electron beams and demonstrating extreme-ultraviolet free-electron lasers. *Phys. Rev. Res.* **8**, 013207 (2026).

[14] Jiang, K., Wang, W., Feng, K. & Li, R. Review of quality optimization of electron beam based on laser wakefield acceleration. *Photonics* **9**, 511 (2022).

[15] Maier, A. R. et al. Decoding sources of energy variability in a laser-plasma accelerator. *Phys. Rev. X* **10**, 031039 (2020).

[16] Wang, W. et al. Free-electron lasing at 27 nanometres based on a laser wakefield accelerator. *Nature* **595**, 516-520 (2021).

[17] Kando, M., Hosokai, T., Kim, K. Y. & Tang, C. Facilities in Asia for future accelerator development. *JINST* **17**, T06001 (2022).

[18] Lei, Z. et al. Controllable electron self-injection in laser wakefield acceleration with asymmetric gas-jet nozzle. *Prog. Theor. Exp. Phys.* **2023**, 033J01 (2023).

[19] Nakanii, N., Huang, K., Kondo, K., Kiriyama, H. & Kando, M. Precise pointing control of high-energy electron beam from laser wakefield acceleration using an aperture. *Appl. Phys. Express* **16**, 026001 (2023).

[20] Huang, K., Jin, Z., Nakanii, N., Hosokai, T. & Kando, M. Electro-optic 3D snapshot of a laser wakefield accelerated kilo-ampere electron bunch. *Light Sci. Appl.* **13**, 84 (2024).

[21] Buck, A. et al. Shock-front injector for high-quality laser-plasma acceleration. *Phys. Rev. Lett.* **110**, 185006 (2013).

[22] Del Sarto, D. et al. A systematic investigation on the response of EBT-XD gafchromic films to varying dose-per-pulse, average dose-rate and instantaneous dose-rate in electron flash beams. *Front. Phys.* **13**, 1474416 (2025).

[23] Buxton, G. V. & Stuart, C. R. Re-evaluation of the thiocyanate dosimeter for pulse radiolysis. *J. Chem. Soc. Faraday Trans.* **91**, 279-281 (1995).

[24] Yang, J., Kondoh, T., Kan, K. & Yoshida, Y. Ultrafast pulse radiolysis. *Nucl. Instrum. Methods Phys. Res. A* **629**, 6-10 (2011).

[25] Kato, R. et al. Upgrade of the L-band linac at ISIR, Osaka University for highly stable operation in *Free Electron Lasers 2003: Proceedings of the 25th International Free Electron Laser Conference and the 10th FEL Users Workshop* (eds. Minehara, E. J., Sawamura, M. & Hajima, R.) II-43–II-44 (Elsevier, 2004).

[26] Sato, T. et al. Features of Particle and Heavy Ion Transport code System (PHITS) version 3.02. *J. Nucl. Sci. Technol.* **55**, 684-690 (2018).

[27] Lehe, R., Kirchen, M., Andriyash, I. A., Godfrey, B. B. & Vay, J.-L. A spectral, quasi-cylindrical and dispersion-free particle-in-cell algorithm. *Comput. Phys. Commun.* **203**, 66-82 (2016).

[28] Tanaka, T. SIMPLEX: simulator and postprocessor for free-electron laser experiments. *J. Synchrotron Radiat.* **22**, 1319-1326 (2015).

[29] Trofymenko, S. V. & Shul'ga, N. F. Energy loss by relativistic electron ensembles due to coherent excitation and ionization of atoms. *Phys. Rev. Accel. Beams* **23**, 084501 (2020).

Figure captions

Figure 1 | Experimental setups for electron beam generation, transport, and irradiation.

(a) Laser wakefield acceleration (LWFA) platform used for ultrashort, high-energy electron beam transport and beam-induced chemical activation in deep aqueous media. Representative target configurations used for depth-dependent dose measurements using Gafchromic films, model substrate activation in sealed vials, and pulse-radiolysis-based KSCN chemical dosimetry using a 450 nm laser diode are illustrated schematically. The previously installed XUV free-electron laser (FEL) undulator section is shown for reference, as previous FEL amplification experiments on the same beamline provide an experimentally validated benchmark for stable transport of high-quality LWFA electron beams to the target region. The undulator gap was fully opened and the section was not used during the present irradiation experiments.

(b) Conventional L-band radio-frequency (RF) accelerator platform used for chemical and functional validation experiments. Schematic views illustrate the beam transport geometry, pulse-radiolysis-based KSCN chemical dosimetry configuration using a Xe flash lamp and spectrometer system, and representative target configurations used for model substrate activation, cellular experiments, and in vivo studies in a cancer mouse model.

Figure 2 | Shot-to-shot stability of the LWFA electron beam platform used for deep-water interaction experiments.

(a) Beam centroid positions measured over 50 consecutive shots using the S1 phosphor-screen monitor (Figure 1a), located approximately 1 m downstream from the LWFA source, demonstrating stable beam pointing. The PMQ optics were retracted from the beam path during this measurement to directly evaluate the intrinsic source pointing stability.

(b) Electron beam charge measured over the same 50-shot sequence, confirming reproducible charge delivery for downstream dosimetric and chemical analyses.

(c) Central electron beam energy measured over the same 50-shot sequence, demonstrating stable quasi-monoenergetic beam generation.

(d) Overlaid electron energy spectra obtained over the same 50-shot sequence, showing reproducible energy spectra with a narrow energy spread.

Figure 3 | Deep-water transport behavior of LWFA electron beams and depth-dependent beam-induced chemistry.

(a) Depth-dependent dose deposition measured using Gafchromic films at representative depths (0, 1, 2, 3, 4, 5, 6, 7, 8, 9, 10, 12, 14, 16, 18, and 20 cm) within a 20 cm-thick water target positioned approximately 7 m downstream from the LWFA source. Dose values were obtained by integrating the central beam region using a 200 μm-diameter analysis window and are reported as area-averaged absorbed doses. The absorbed dose at the water-target entrance ($z = 0$ cm) within the 200 μm-diameter analysis region was estimated to be approximately 1.8 Gy per LWFA shot. Experimental data represent the average of four independently accumulated 10-shot datasets. Both the experimental and Monte Carlo profiles were normalized to their respective values at the water-target entrance to compare the depth-dependent behavior of the central beam component.

(b) Depth-dependent dose deposition obtained using a 10 mm-diameter integration window. The absorbed dose at the water-target entrance within the 10 mm-diameter analysis region was estimated to be approximately 0.08 Gy per LWFA shot. Experimental data represent the average of four independently accumulated 10-shot datasets. Both the experimental and Monte Carlo profiles were normalized to their respective values at the water-target entrance. The resulting profile represents the depth-dependent behavior of the overall beam transport through the water target.

(c) Evolution of the beam diameter (FWHM) during propagation through the water target, determined from Gafchromic film measurements. Data represent the average of four independently accumulated 10-shot datasets.

(d) Depth-dependent azide-to-amine conversion of the model substrate (azide 1) measured in sealed vials positioned along the beam axis within the water target. The four vial samples corresponded to depth ranges of 0.5–5.0 cm, 5.5–10.0 cm, 10.5–15.0 cm, and 15.5–20.0 cm, respectively. Chemical analysis was performed using samples accumulated over 200 LWFA shots. The observed conversion profile demonstrates that beam-triggered reductive chemistry remains inducible after deep-water propagation of the LWFA electron beam.

Figure 4 | Reduction reaction of phenyl azide 1 as a model reaction for beam-triggered prodrug activation.

a, Reduction reaction of phenyl azide **1** to amine **2**.
b, UPLC traces showing conversion of azide **1** (retention time: 4.45 min) to amine **2** (retention time: 2.08 min) after 60 Gy irradiation.
c, Yield of amine **2** as a function of irradiation dose (0–60 Gy), determined from UPLC calibration curves. Data are presented as mean ±s.d. (n = 3).

Figure 5 | Activation of doxorubicin prodrug 3 by electron beam irradiation.

a, Schematic illustration of prodrug activation.
b, UPLC traces showing conversion of prodrug **3** (retention time: 6.09 min) to doxorubicin (retention time: 3.81 min) after 40 Gy irradiation (1.0 Gy per pulse, 40 pulses).

Figure 6 | Effect of electron beam irradiation on cancer cell viability.

a, Experimental workflow. HeLa cells were seeded into vials and incubated for 24 h, followed by assignment to four groups: untreated control (CTRL), prodrug **3** alone (Prodrug), electron beam irradiation alone (EB), and combined treatment (Prodrug+EB). Electron beams were delivered using an L-band linear accelerator. Cell viability was assessed using the AlamarBlue™ assay after 72 h of incubation at 37 °C.

b, Viability of HeLa cells following treatment with electron beams from the L-band linear accelerator (27 MeV, total dose 4.4 Gy, 1.1 Gy per pulse, 4 pulses). Data are shown as mean ±s.d. (n = 3). Green, no electron beam (CTRL and Prodrug); blue, EB irradiation.

Figure 7 | In vivo response to electron beam–triggered chemical activation

a, Schematic of the in vivo experimental design. HeLa tumor–bearing BALB/c nude mice were subcutaneously administered prodrug **3**. Four hours later, mice were either irradiated or not irradiated with an electron beam (27 MeV, total dose 4.0 Gy, 1.0 Gy per pulse, 4 pulses) using an L-band linear accelerator.

b, Tumor weight measured four weeks after treatment. Data are presented as mean ±s.d. (n = 5). *P < 0.05 (Tukey's test); the asterisk indicates statistical significance relative to the EB group.

Figure 8 | Conceptual illustration of beam-triggered chemical activation in deep biological media.

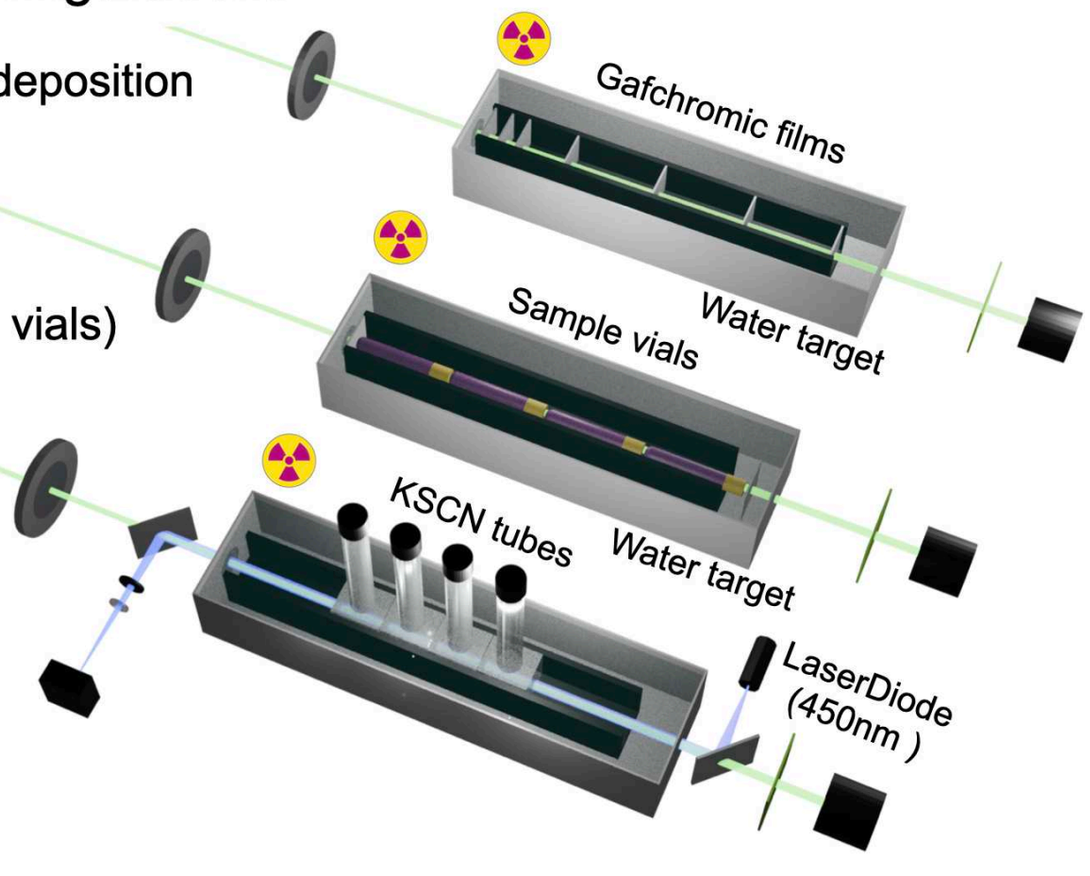
The schematic illustrates a conceptual framework in which very-high-energy electron (VHEE) beams penetrate deep into biological media and trigger localized chemical activation of administered prodrugs, leading to localized biological responses at the irradiation site. It summarizes the conceptual link between deep electron-beam transport and energy deposition, chemical activation, and subsequent biological response explored in the present study. The illustration is intended to convey the underlying physical and chemical concepts rather than depict a clinical implementation.

Representative Target Configurations

(i) The depth-dependent dose deposition
(Gafchromic films)

(ii) The Chemical reaction
(a model substrate in sealed vials)

(iii) Pulse-radiolysis-based
KSCN chemical dosimeter



Ti:Sapphire laser
Beamline 2 of *LAPLACIAN*

- λ = 800 nm,
- 600 mJ / Pulse
- 24 fs (FWHM)

Figure 1 a

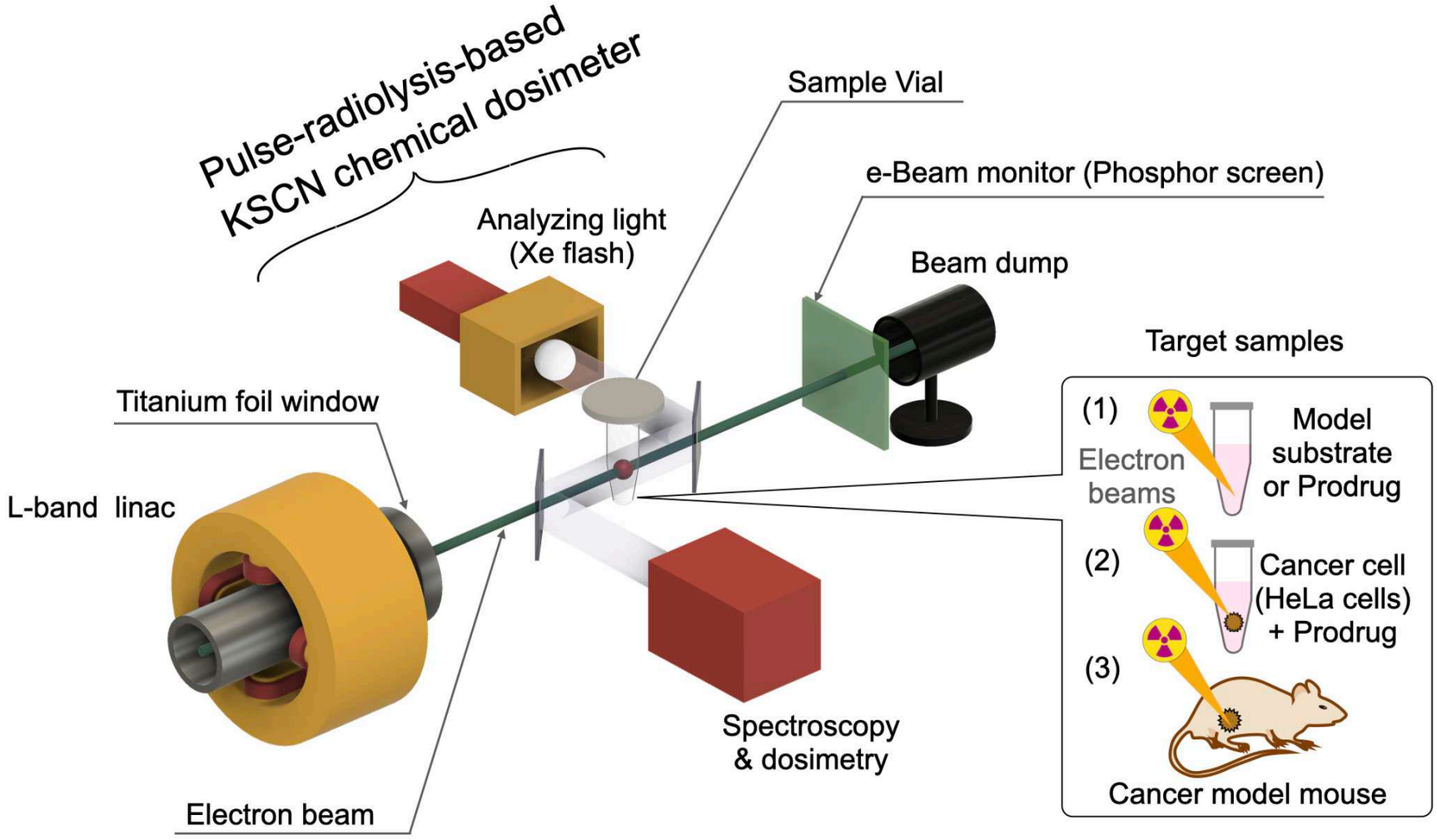
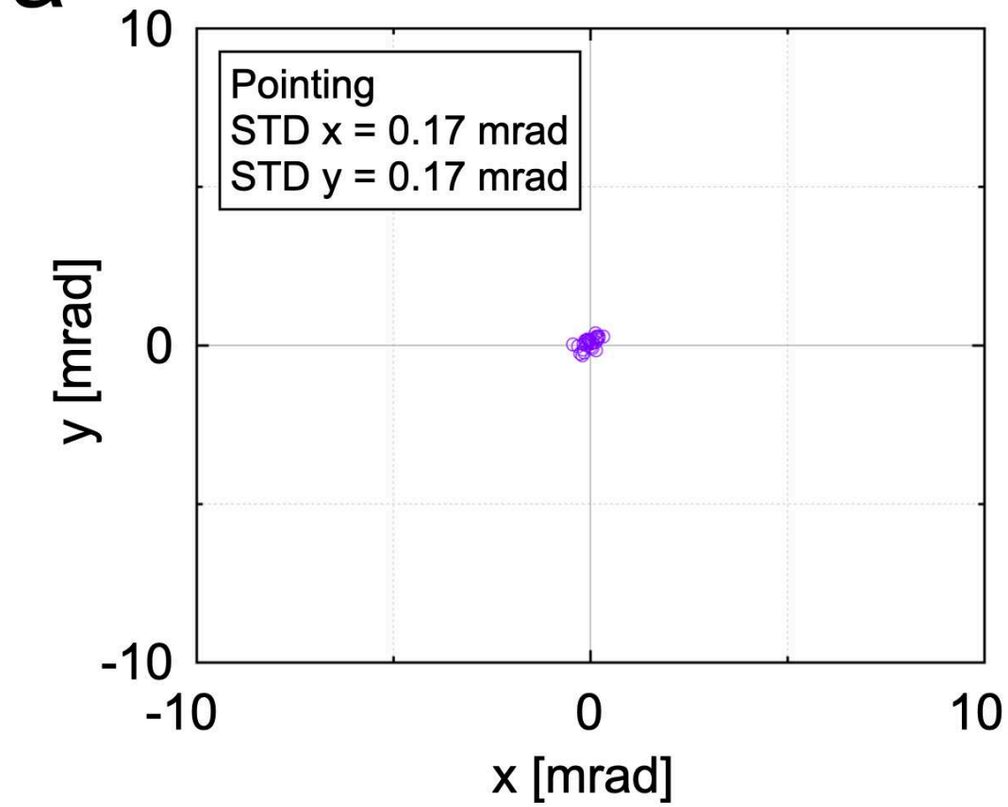
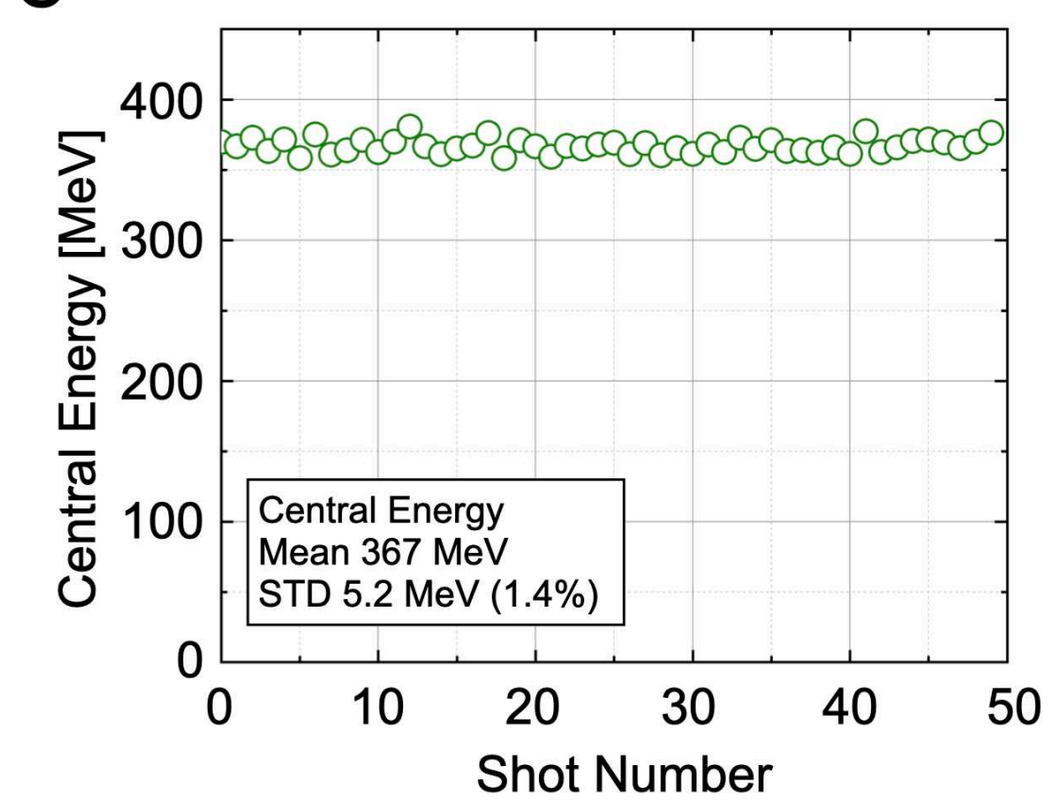
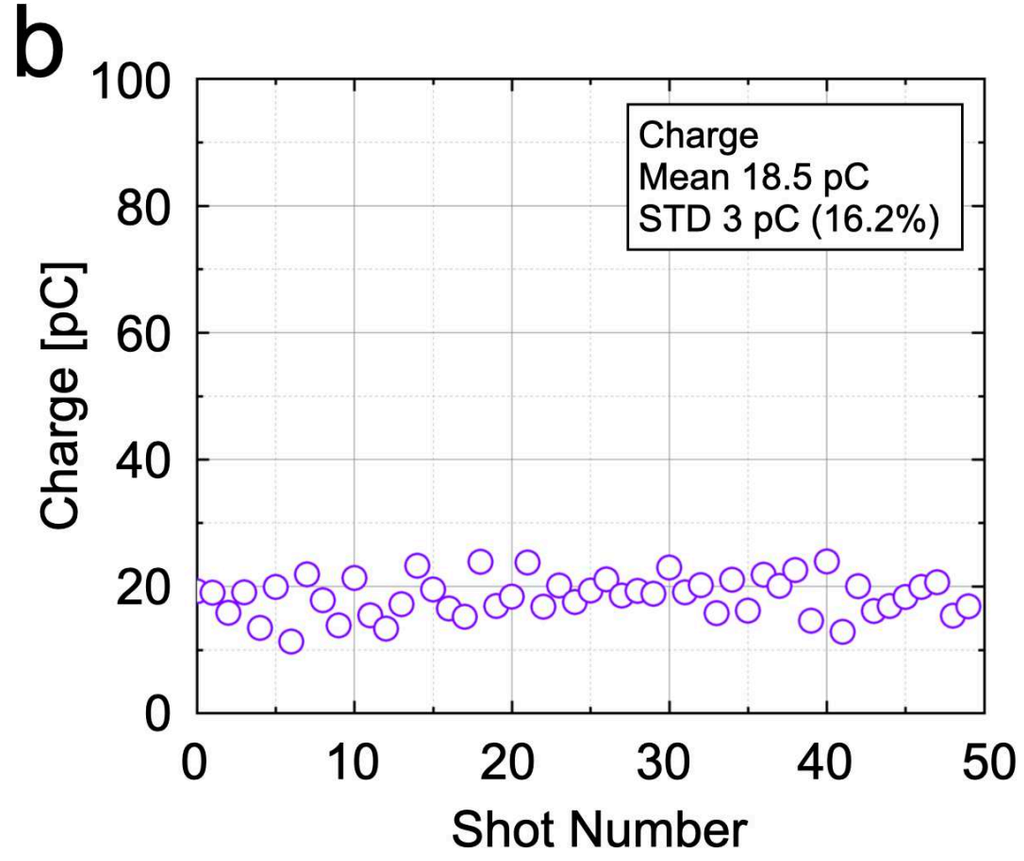

Pulse-radiolysis-based
KSCN chemical dosimeter
Sample Vial
e-Beam monitor (Phosphor screen)
Analyzing light
(Xe flash)
Beam dump
Target samples
Titanium foil window
(1)
Electron
beams
Model
substrate
or Prodrug
L-band linac
(2)
Cancer cell
(HeLa cells)
+ Prodrug
(3)
Spectroscopy
& dosimetry
Electron beam
Cancer model mouse

Figure 1 b


a
Pointing
STD x = 0.17 mrad
STD y = 0.17 mrad
y [mrad]
x [mrad]
10
0
-10
-10
0
10


c
Central Energy
Mean 367 MeV
STD 5.2 MeV (1.4%)
Central Energy [MeV]
Shot Number
400
300
200
100
0
0
10
20
30
40
50


b
Charge
Mean 18.5 pC
STD 3 pC (16.2%)
Charge [pC]
Shot Number
100
80
60
40
20
0
0
10
20
30
40
50

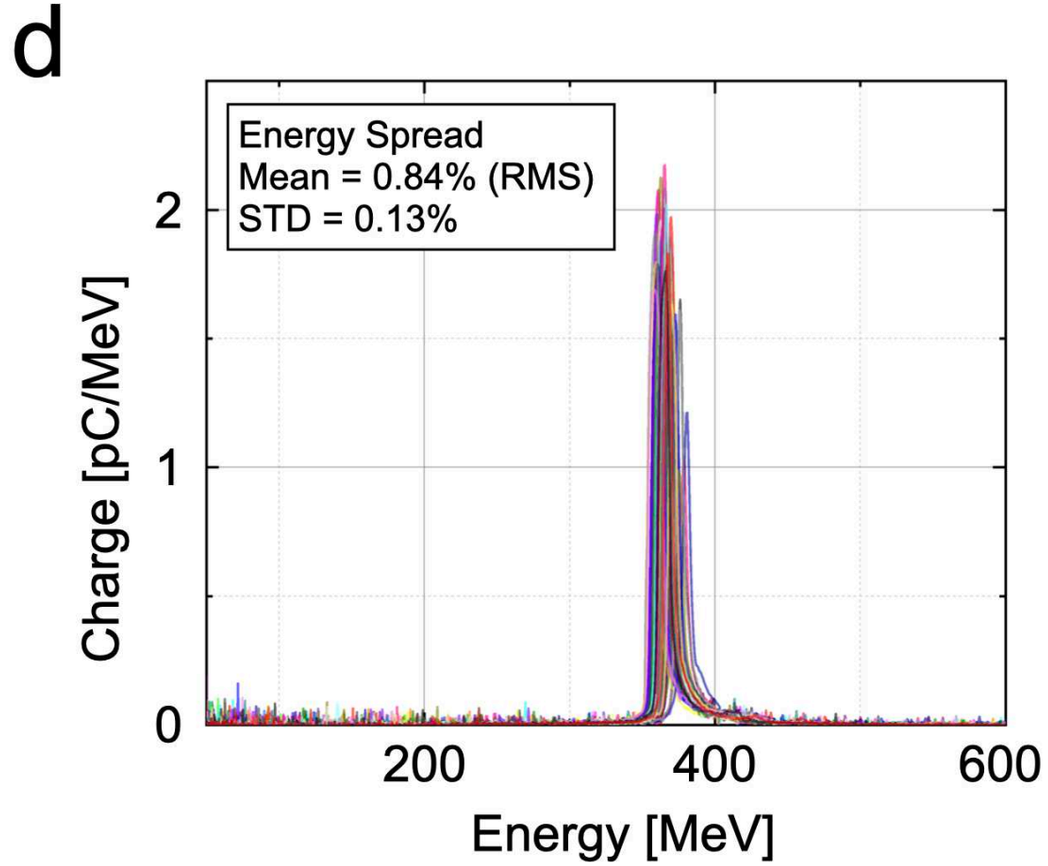
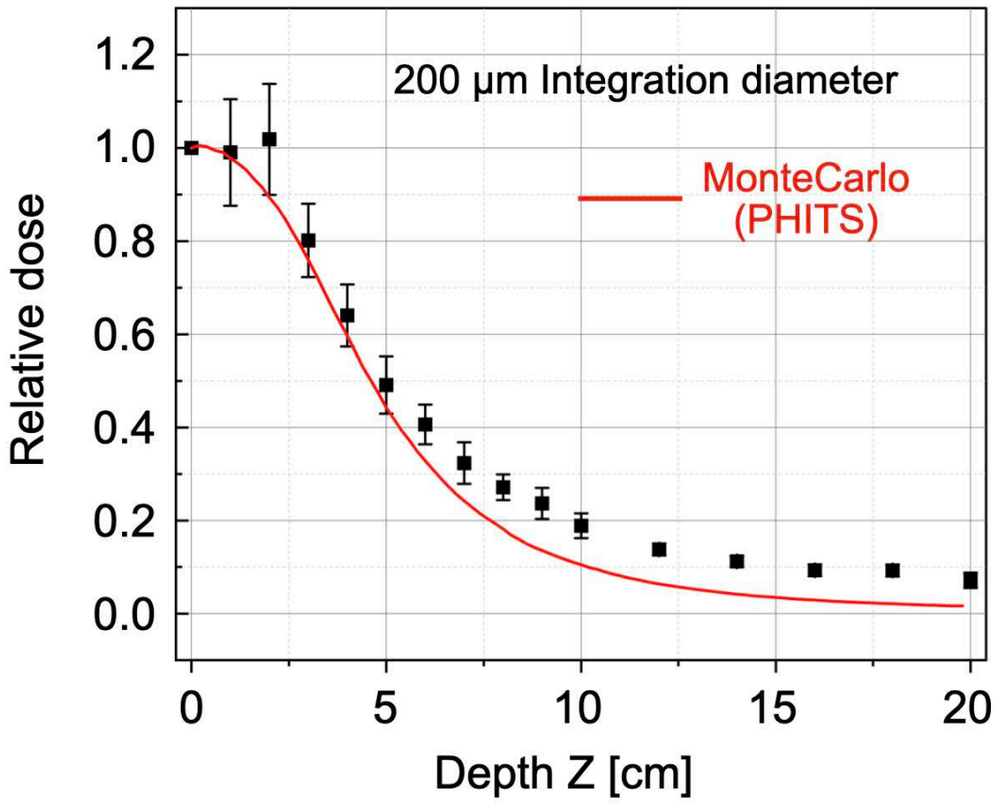
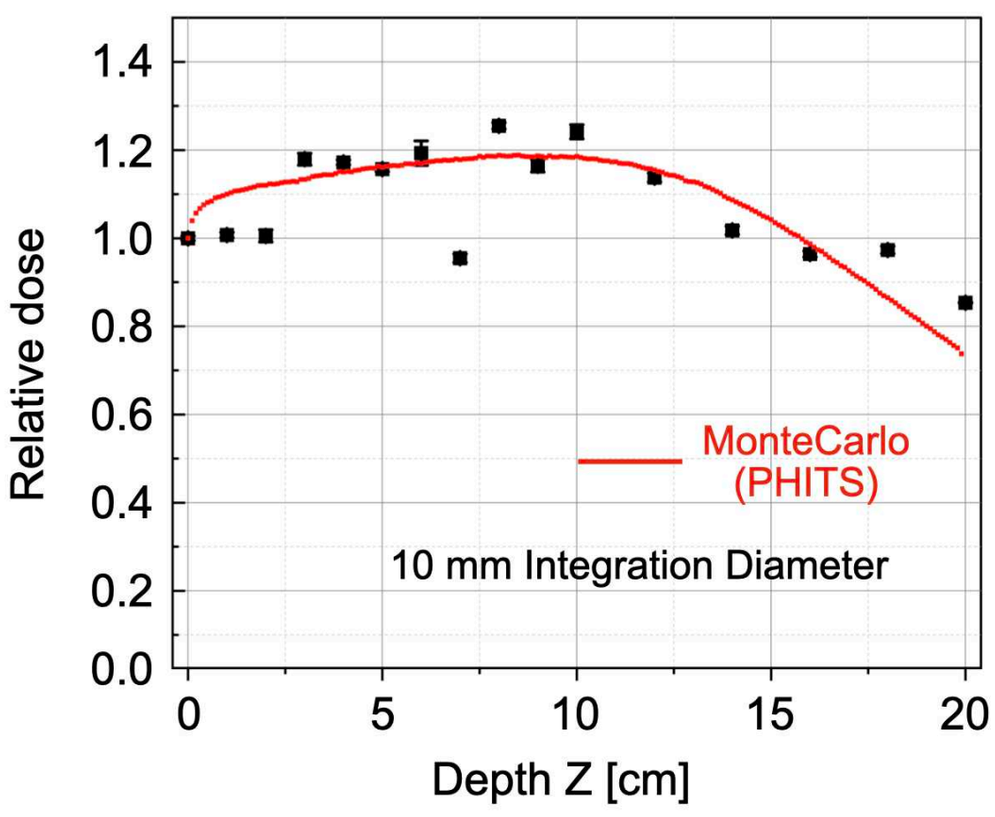

d
Energy Spread
Mean = 0.84% (RMS)
STD = 0.13%
Charge [pC/MeV]
Energy [MeV]
2
1
0
200
400
600

Figure 2

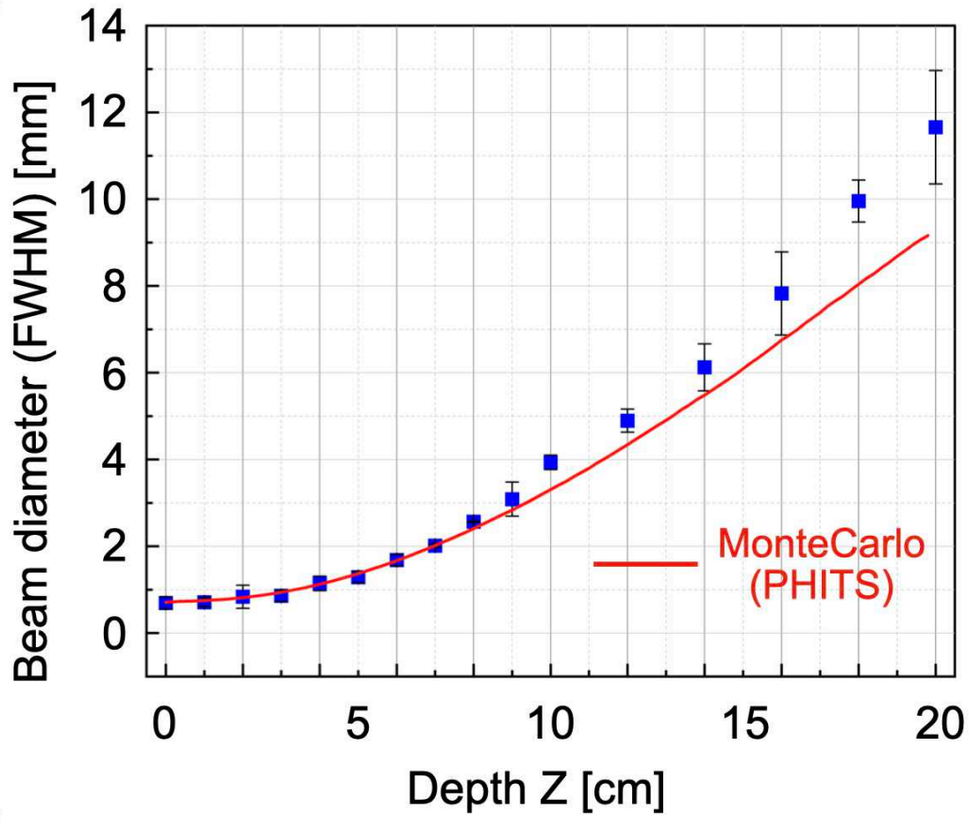
a



b



c



d

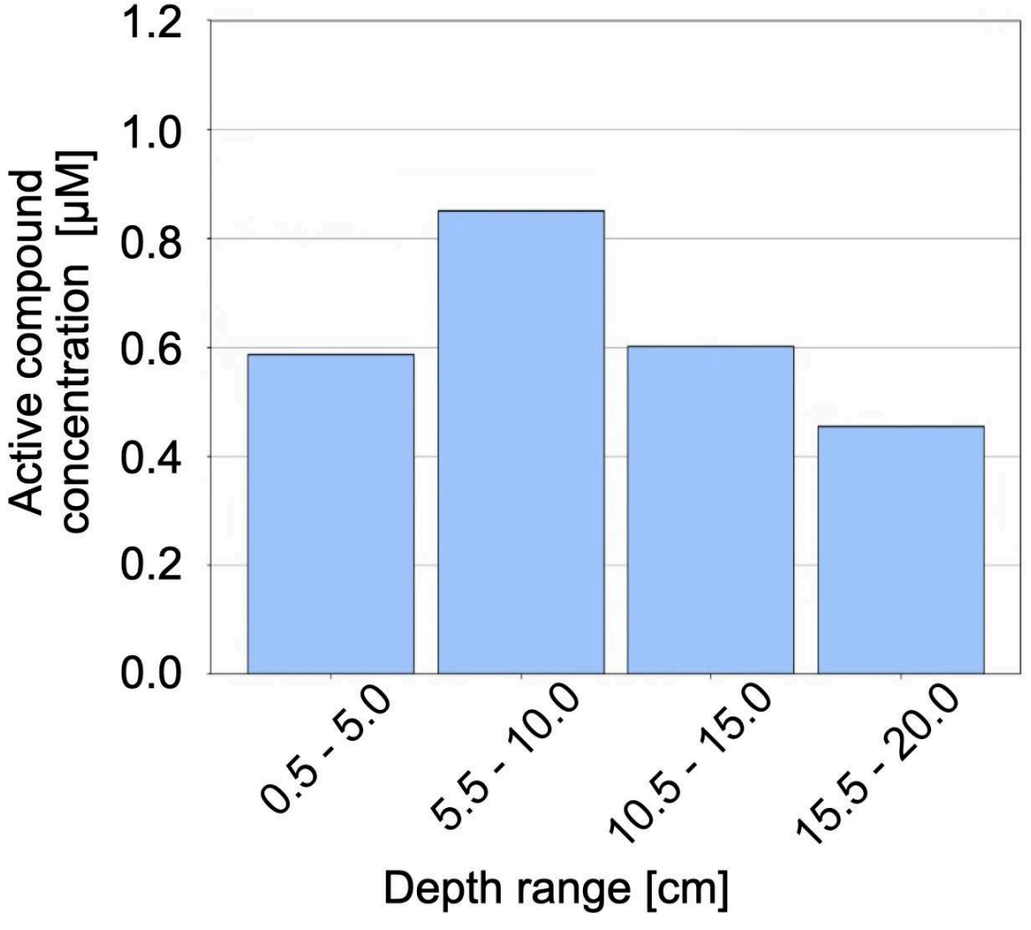
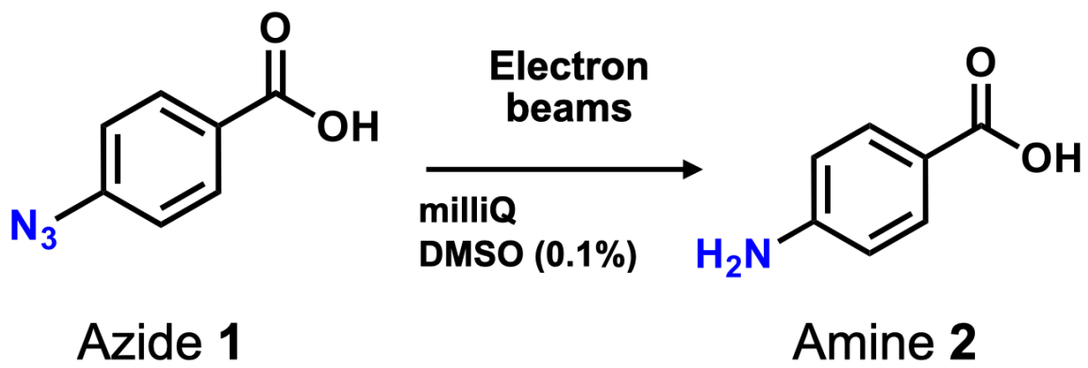


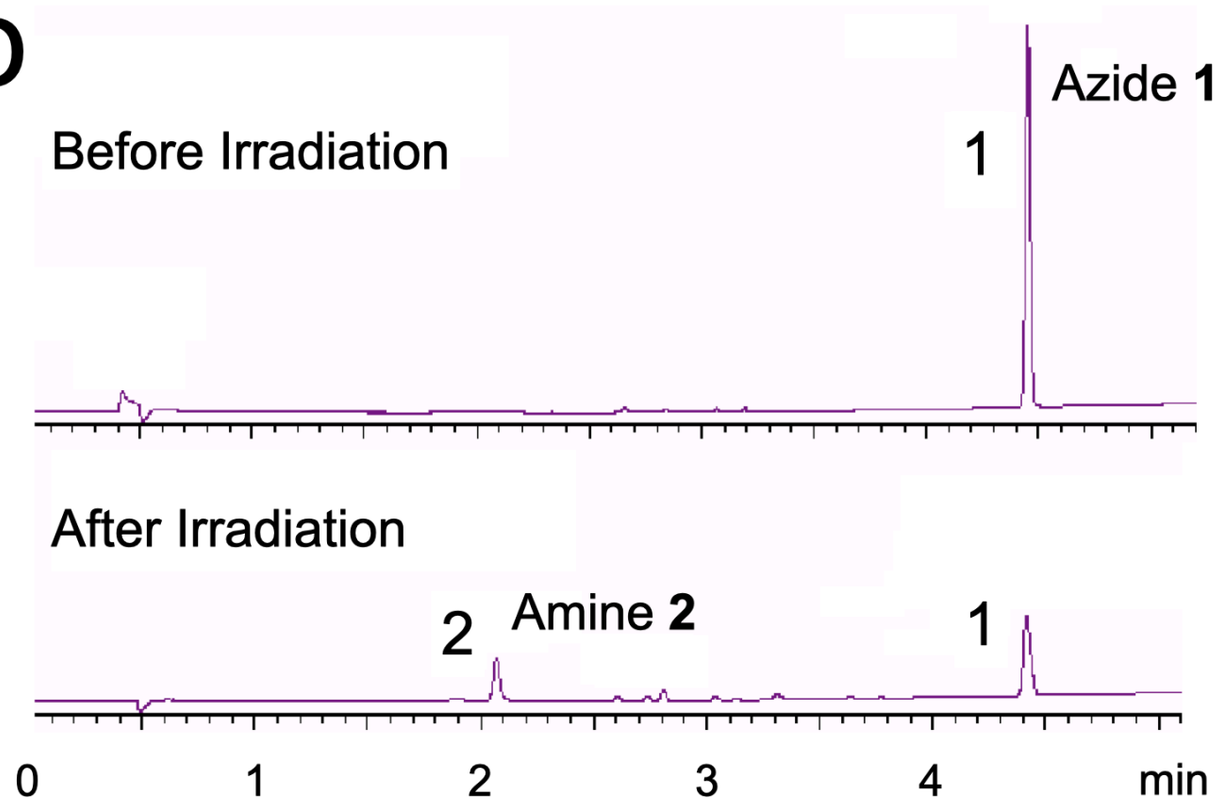
Figure 3

a



Azide **1** Amine **2**

b



c

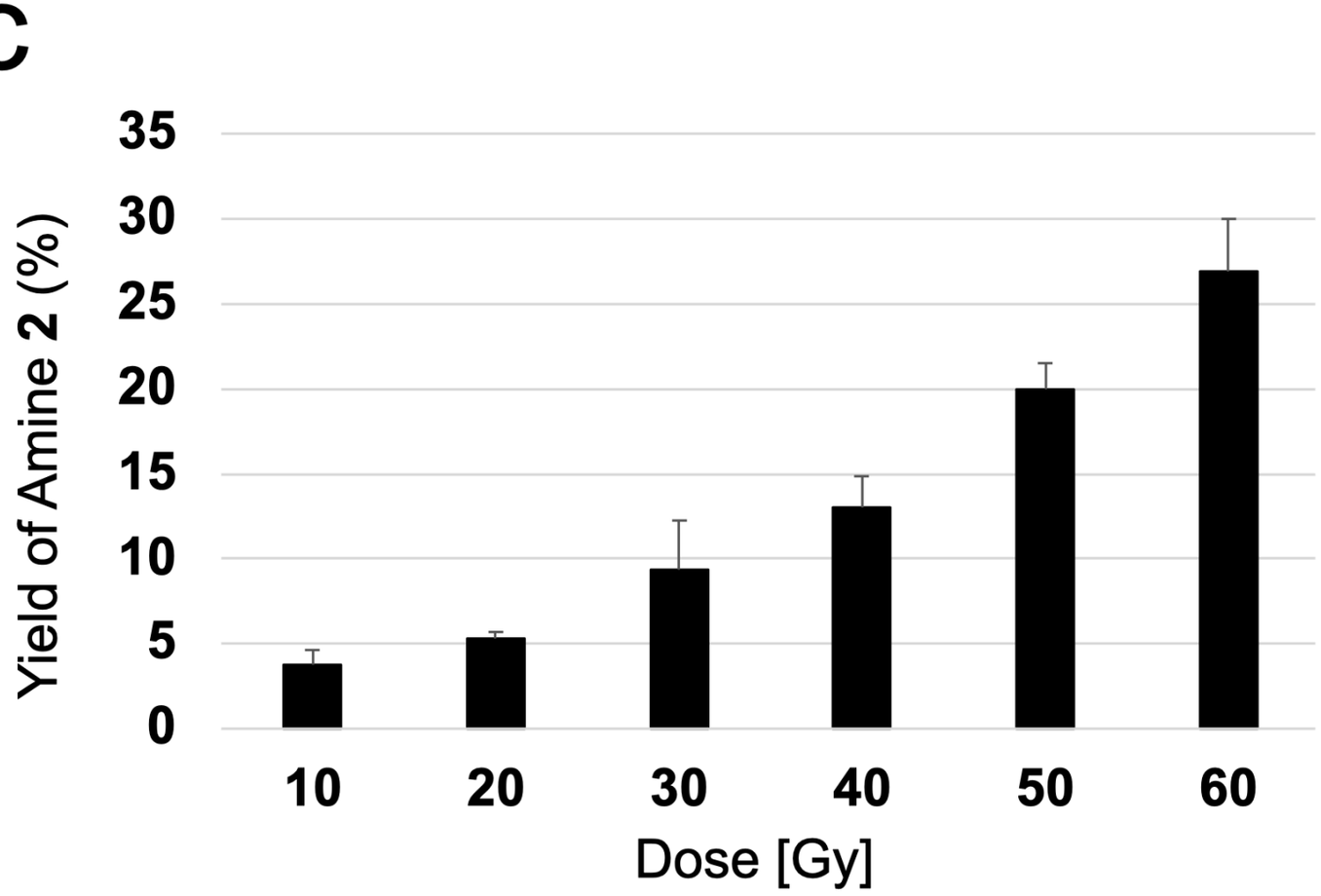
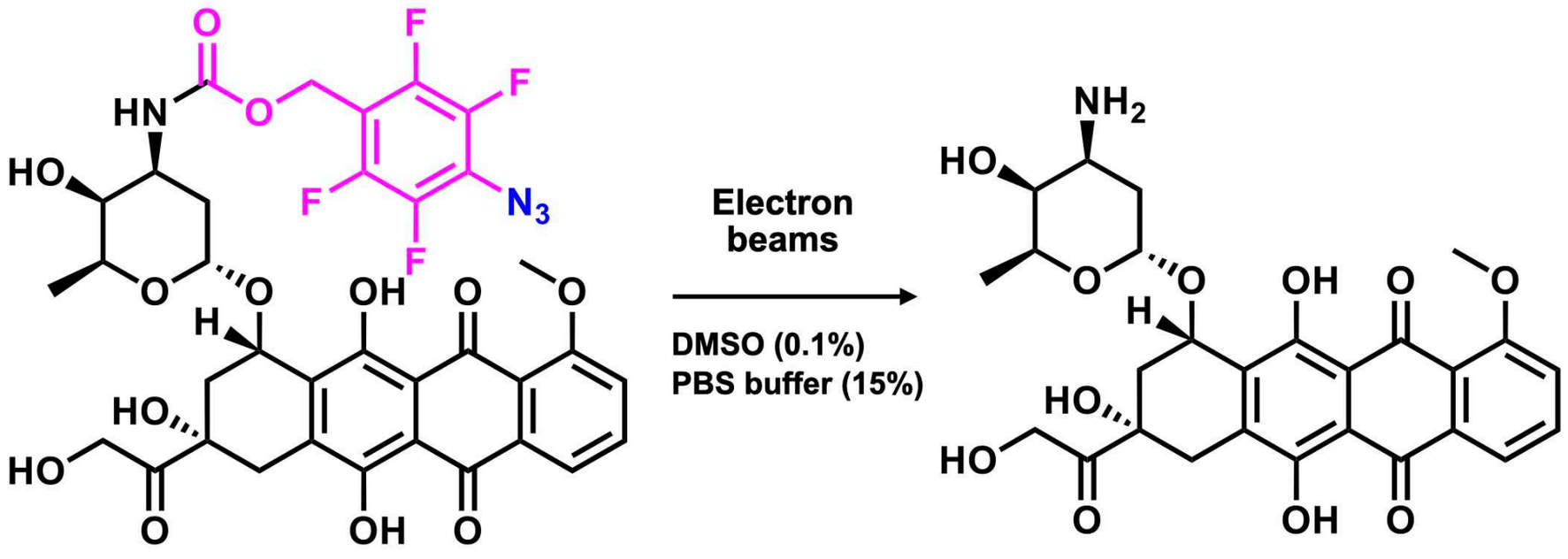


Figure 4

a



Prodrug **3**

Doxorubicin

b

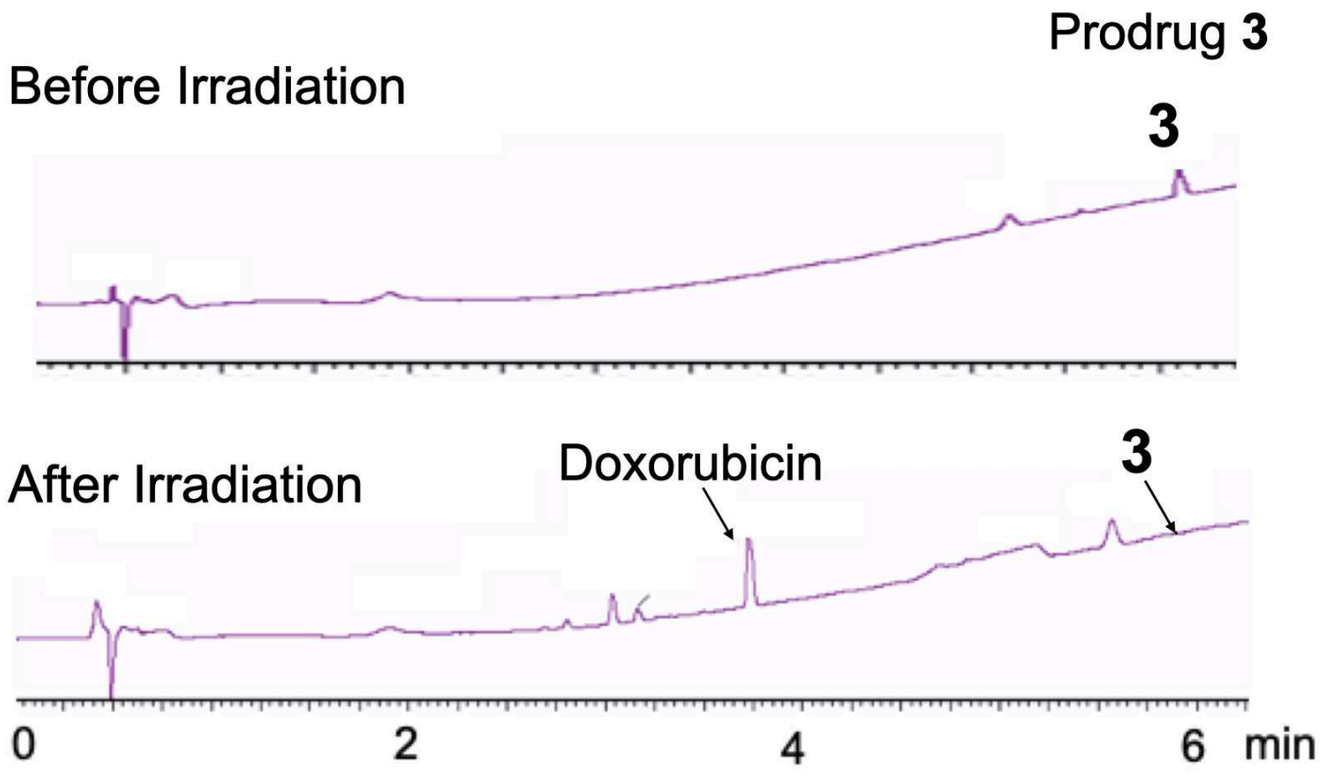
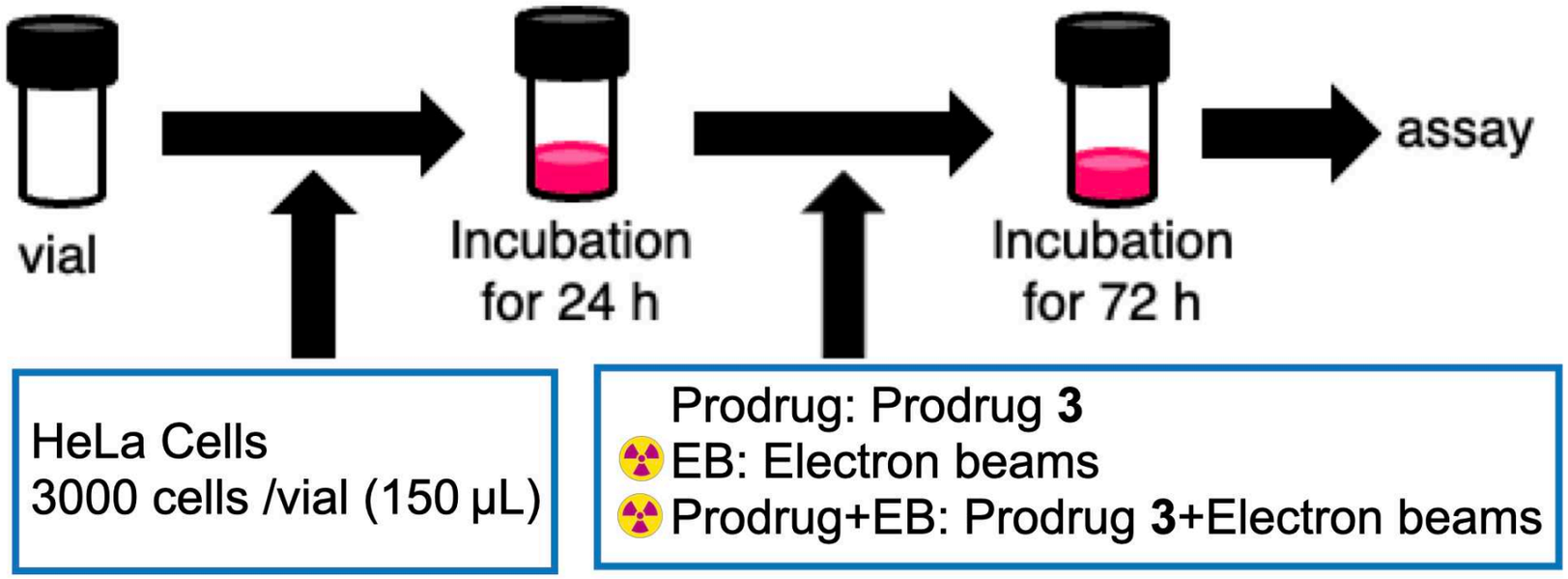


Figure 5

a


vial
Incubation
for 24 h
Incubation
for 72 h
assay
HeLa Cells
3000 cells /vial (150 μL)
Prodrug: Prodrug 3
EB: Electron beams
Prodrug+EB: Prodrug 3+Electron beams

b

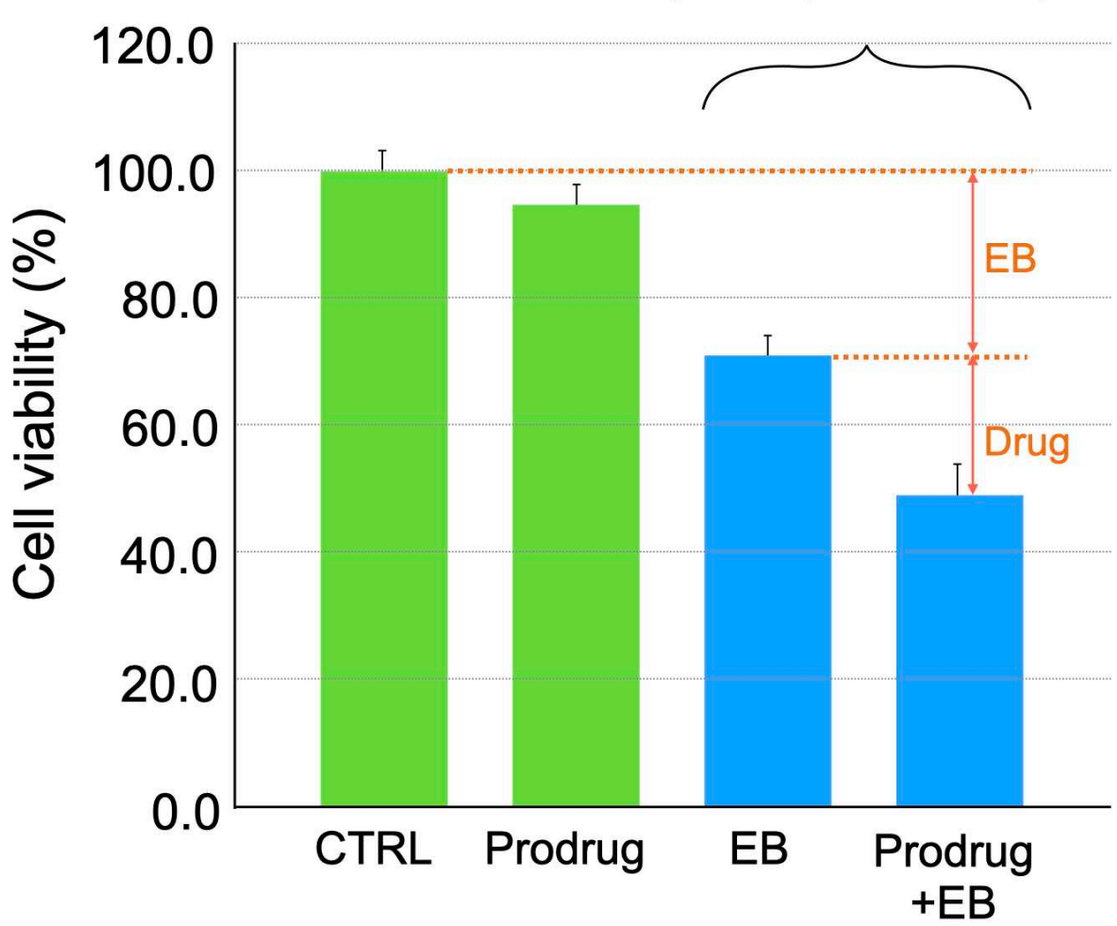
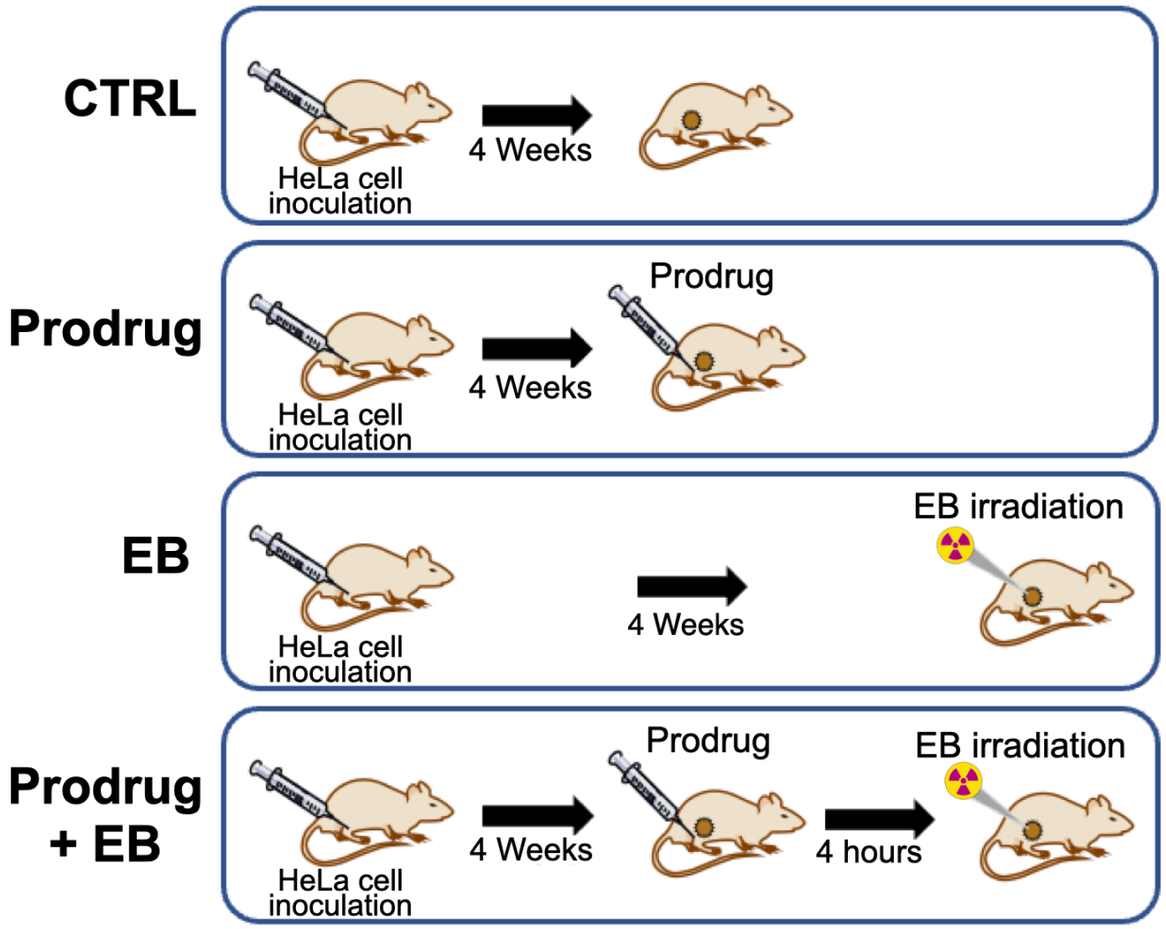

4.4Gy
(1.1 Gy/Pulse x 4)
Cell viability (%)
120.0
100.0
80.0
60.0
40.0
20.0
0.0
EB
Drug
CTRL
Prodrug
EB
Prodrug
+EB

Figure 6

a


CTRL
HeLa cell inoculation
4 Weeks
Prodrug
HeLa cell inoculation
4 Weeks
Prodrug
EB
HeLa cell inoculation
4 Weeks
EB irradiation
Prodrug + EB
HeLa cell inoculation
4 Weeks
Prodrug
4 hours
EB irradiation

b

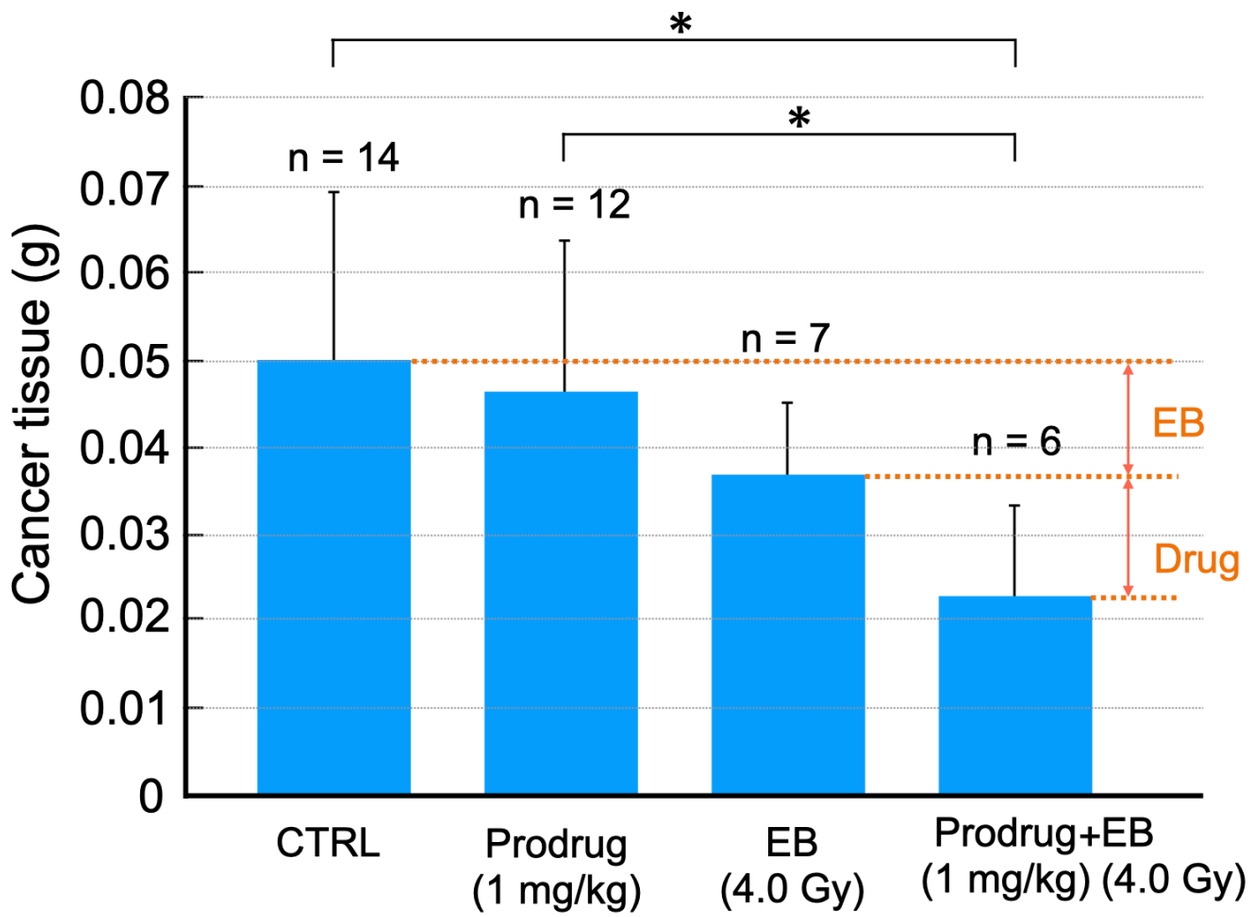

*
*
n = 14
n = 12
n = 7
n = 6
EB
Drug
Cancer tissue (g)
0.08
0.07
0.06
0.05
0.04
0.03
0.02
0.01
0
CTRL
Prodrug (1 mg/kg)
EB (4.0 Gy)
Prodrug+EB (1 mg/kg) (4.0 Gy)

Figure 7

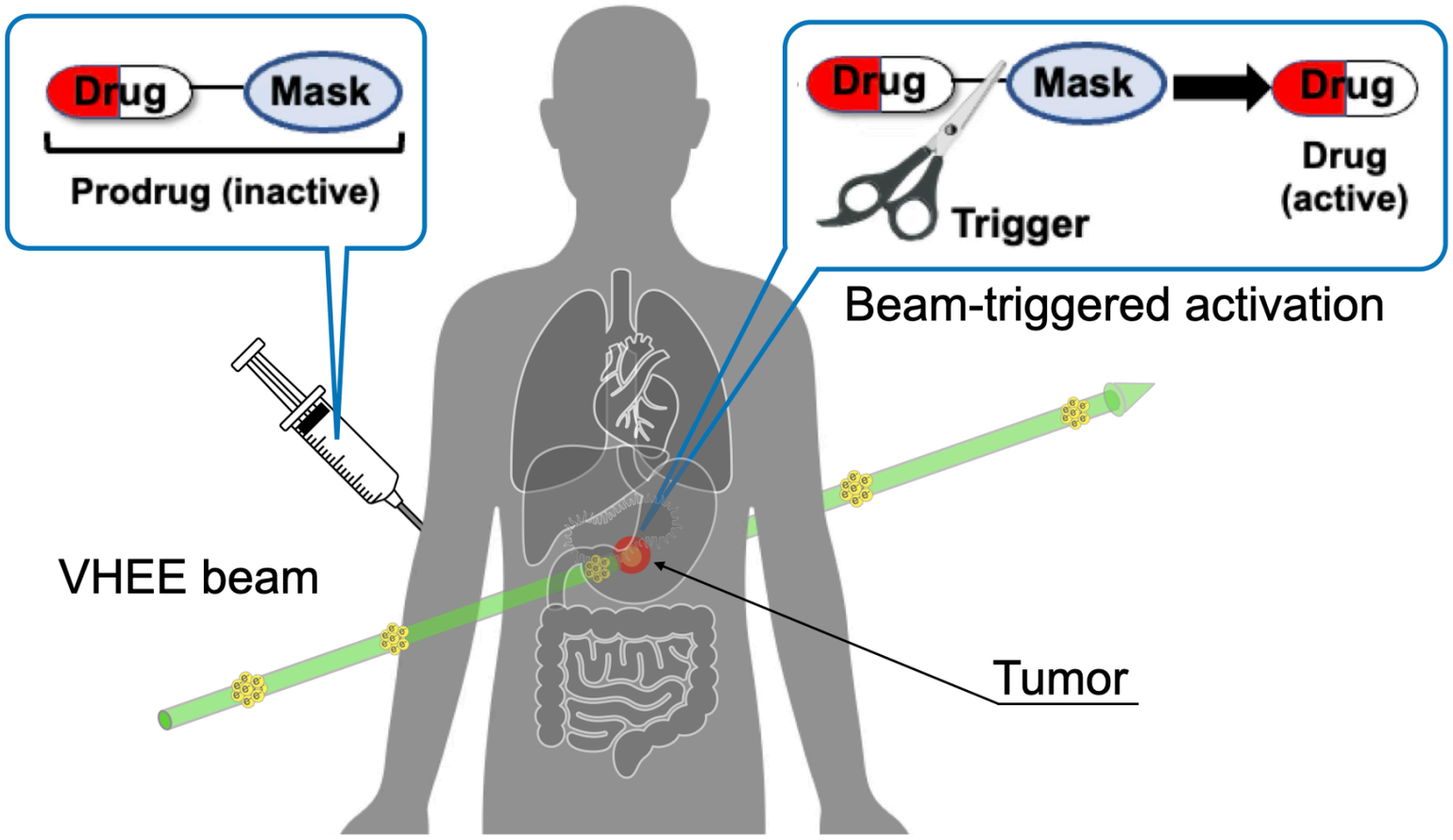

Drug
Mask
Prodrug (inactive)
Drug
Mask
Drug
Drug
(active)
Trigger
Beam-triggered activation
VHEE beam
Tumor

Figure 8

Supplementary Files

This is a list of supplementary files associated with this preprint. Click to download.

- SupplementaryFigures.pdf
- SupplementaryInfo.docx